Physics of Plasmas

Vertical profiles and two-dimensional distributions of carbon line emissions from C^{2+}–C^{5+} ions in attached and RMP-assisted detached plasmas of large helical device

Cite as: Phys. Plasmas **24**, 022510 (2017); https://doi.org/10.1063/1.4976989
Submitted: 12 August 2016 • Accepted: 07 February 2017 • Published Online: 28 February 2017

Hongming Zhang, Shigeru Morita, Shuyu Dai, et al.

View Online Export Citation CrossMark

ARTICLES YOU MAY BE INTERESTED IN

Detachment stabilization with $n/m = 1/1$ resonant magnetic perturbation field applied to the stochastic magnetic boundary of the Large Helical Device
Physics of Plasmas **17**, 056111 (2010); https://doi.org/10.1063/1.3368681

Performance of Wendelstein 7-X stellarator plasmas during the first divertor operation phase
Physics of Plasmas **26**, 082504 (2019); https://doi.org/10.1063/1.5098761

Impurity confinement and transport in high confinement regimes without edge localized modes on DIII-D
Physics of Plasmas **22**, 055901 (2015); https://doi.org/10.1063/1.4918359



AIP Publishing

© 2017 Author(s).

Vertical profiles and two-dimensional distributions of carbon line emissions from $C^{2+}-C^{5+}$ ions in attached and RMP-assisted detached plasmas of large helical device

Hongming Zhang,[1] Shigeru Morita,[1,2] Shuyu Dai,[2,3] Tetsutarou Oishi,[1,2] Motoshi Goto,[1,2] Xianli Huang,[2] Gakushi Kawamura,[1,2] Masahiro Kobayashi,[1,2] Yang Liu,[1] Izumi Murakami,[1,2] Yoshiro Narushima,[1,2] and LHD Experimental Group

[1]*Department of Fusion Science, Graduate University for Advanced Studies, Toki 509-5292, Gifu, Japan*
[2]*National Institute for Fusion Science, Toki 509-5292, Gifu, Japan*
[3]*Key Laboratory of Materials Modification by Laser, Ion and Electron Beams (Ministry of Education), School of Physics and Optoelectronic Technology, Dalian University of Technology, Dalian 116024, People's Republic of China*

(Received 12 August 2016; accepted 7 February 2017; published online 28 February 2017)

In Large Helical Device (LHD), the detached plasma is obtained without external impurity gas feed by supplying an m/n = 1/1 resonant magnetic perturbation (RMP) field to a plasma with an outwardly shifted plasma axis position of $R_{ax} = 3.90$ m where the magnetic resonance exists in the stochastic magnetic field layer outside the last closed flux surface. The plasma detachment is triggered by the appearance of an m/n = 1/1 island when the density, increased using hydrogen gas feed, exceeds a threshold density. The behavior of intrinsically existing impurities, in particular, carbon originating in the graphite divertor plates, is one of the important key issues to clarify the characteristic features of the RMP-assisted plasma detachment although the particle flux still remains on some divertor plates even in the detachment phase of the discharge. For this purpose, vertical profiles and two-dimensional (2-D) distributions of edge carbon emissions of CIII to CVI have been measured at extreme ultraviolet wavelength range, and the results are compared between attached and RMP-assisted detached plasmas. It is found that the CIII and CIV emissions located in the stochastic magnetic field layer are drastically increased near the m/n = 1/1 island O-point and in the vicinity of both inboard and outboard edge separatrix X-points during the RMP-assisted detachment, while those emissions are only enhanced in the vicinity of the outboard edge X-point in attached plasmas without RMP. The result clearly indicates a change in the magnetic field lines connecting to the divertor plates, which is caused by the growth of the m/n = 1/1 edge magnetic island. In contrast, the intensity of CVI emitted radially inside the magnetic island significantly decreases during the detachment, suggesting an enhancement of the edge impurity screening. The measured carbon distribution is analyzed with a three-dimensional edge plasma transport simulation code, EMC3-EIRENE, for the attached plasmas without RMP. It is found that the narrow strip-shaped impurity trace emitted along the edge X-point and its width are sensitive to the cross-field impurity diffusion coefficient, $D_{Z\perp}$. As a result, the value of $D_{Z\perp}$ of C^{3+} ions is evaluated to be 20 times larger than that of the bulk ions in the $R_{ax} = 3.90$ m configuration, while the reason is unclear at present. The measured 2-D carbon distribution is also discussed and compared to the structure of the m/n = 1/1 magnetic island, which quickly expanded during the appearance of the plasma detachment. *Published by AIP Publishing.* [http://dx.doi.org/10.1063/1.4976989]

I. INTRODUCTION

Heat load mitigation of divertor plates is one of the critical issues for the next-generation device for fusion reactor development such as ITER.[1,2] The peak heat load on ITER divertor plates is expected to exceed 20 MW/m^2, which is almost two times higher than the present engineering limit (~10 MW/m^2).[3] The plasma detachment using the working gas or gaseous impurities, which is a possible solution for the heat load mitigation, has been achieved in many tokamak devices.[4–11] A complete detachment in the H-mode has been achieved without deterioration of the energy confinement in ASDEX Upgrade using a feedback-controlled gas puff system with deuterium and neon. The radiation power reaches 90% of the total input power during the plasma detachment.[5,6] In "hybrid" H-mode plasmas of DIII-D, the peak heat flux at the outer divertor plate is reduced by a factor of 2.5 using argon puffing near the outer divertor target.[7] In the detached H-mode plasma of JT-60U, the power radiated by neon ions at the inner divertor reaches 55% of the total radiation.[8] In JET and Alcator C-Mod, on the other hand, the completely detached H-mode plasmas are successfully obtained using only deuterium gas puff.[9,10]

ITER is expected to operate in the H-mode.[1,2] Therefore, the stability of the edge plasma will be very important in addition to a steady sustainment of the plasma detachment because the large heat flux from edge localized modes (ELMs) may penetrate the edge high radiation region

and reach the divertor plates.[9] At present, however, the operation window of the plasma detachment with the H-mode is narrow.[4–10]

In helical devices, another technique for realizing the detached plasma has been attempted in Wendelstein 7-AS (W7-AS) and in Large Helical Device (LHD) using the resonant magnetic perturbation (RMP) coils without any external impurity gas feed.[12–14] The heat load on divertor plates decreases by a factor of 3–10 during the detachment phase basically without degradation of energy confinement. This method also seems to be attractive for tokamaks because the detached plasma with RMP may mitigate the steady state heat load and eliminate the transient heat load from ELMs.[12] Dedicated experiments have been performed in W7-AS and LHD to investigate the operation window for the steady-state sustainment of high-performance plasmas. In W7-AS, it is found that the island size and magnetic field line pitch in the island at the plasma edge region influence the stability of detached plasmas. In LHD, it is also found that the radial position of the $m/n = 1/1$ island created by RMP is a critical requirement for a successful achievement of the detached plasma. The detached plasma in LHD can only be then achieved when the $m/n = 1/1$ island is created in the edge stochastic magnetic field layer. At present, however, the reason why the radial position of the $m/n = 1/1$ island is so important for the plasma detachment is unclear. In addition, the concentration of impurity iron originating in the first wall protection tiles made of stainless steel is very low in general LHD discharges, particularly in high-density discharges.[15] Carbon released from graphite divertor plates is thought to be a possible impurity source, which can contribute to the high edge radiation during plasma detachment,[12] although the energy loss channel in the RMP-assisted detached plasma still remains an open question. In LHD, therefore, the study of carbon behavior during the plasma detachment is very important to find a cause triggering the detachment transition.

A two-dimensional (2-D) space-resolved EUV spectrometer in LHD has been upgraded to measure the vertical profile and 2-D distribution of impurity line emissions during shorter time intervals in high-power neutral-beam-injection (NBI) discharges with short-pulse lengths of 2–5 s. The upgrade is mainly carried out by increasing the spectrometer scanning speed, installing a thin filter to eliminate the NBI high-energy neutral particles and adopting a new analysis method.[16–18] As a result, it becomes possible to measure the 2-D distribution of impurity emissions from the detached plasmas in the high-power NBI discharge. The influence of the $m/n = 1/1$ magnetic island formed by RMP coils on the edge carbon behavior can then be studied with the upgraded spectrometer system. The NBI discharge shows entirely different behaviors between the two magnetic axis positions of $R_{ax} = 3.75$ m and 3.90 m when the RMP is supplied. The detachment is easily triggered by the RMP when $R_{ax} = 3.90$ m in which the $m/n = 1/1$ island develops just outside the last closed flux surface (LCFS), while the discharge has basically no response to the RMP when $R_{ax} = 3.75$ m in which the island develops just inside the LCFS.[19] On the other hand, the CIII and CIV are located outside the LCFS, and the CV and CVI are located in the vicinity of the LCFS. Therefore, the observation of radial profiles and 2-D distributions of the carbon emissions is very important to study the influence of the island on plasma detachment because the $m/n = 1/1$ island is located just inside and outside the LCFS for the $R_{ax} = 3.75$ m and 3.90 m configurations, respectively. The measured vertical profile and 2-D distribution of carbon emissions are also analyzed using the three-dimensional (3-D) edge plasma transport code, EMC3-EIRENE.

In the present paper, the edge magnetic field structure and the RMP coil system in LHD are described in Sec. II. EUV spectroscopy and VUV spectroscopy are briefly explained in Sec. III. Then, the vertical profile and 2-D distribution of impurity carbon emissions from NBI discharges at $R_{ax} = 3.75$ m and 3.90 m are presented with data analysis by the simulation in Secs. IV and V, respectively. Finally, the study is summarized in Sec. VI.

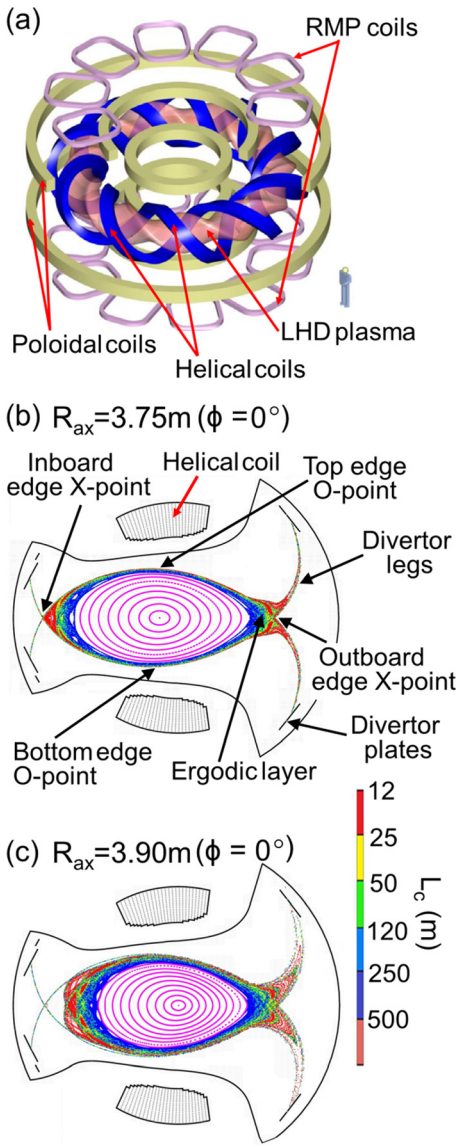


FIG. 1. (a) Bird's eye view of helical coils, poloidal coils, RMP coils, and toroidal plasma shape in LHD and connection lengths (L_c) in the ergodic layer with a magnetic axis of (b) $R_{ax} = 3.75$ m and (c) $R_{ax} = 3.90$ m.

II. EDGE ISLAND FORMATION BY RMP COILS IN LHD

The magnetic field for plasma confinement in LHD is produced by two superconducting helical coils with poloidal and toroidal pitch numbers of $l = 2$ and $n = 10$, respectively, as shown in Fig. 1(a), while three pairs of superconducting poloidal coils are used for the control of the plasma position, the shaping of the plasma cross section, and the cancelling of the stray magnetic field. The major radius of the magnetic axis position can be varied between $R_{ax} = 3.50$ and 4.00 m.[20] The averaged plasma minor radius defined by the LCFS takes the maximum value of 64 cm when $R_{ax} = 3.60$ m. The core plasma in LHD is always accompanied by a stochastic magnetic layer called the "ergodic layer" formed outside the LCFS, which originates in the presence of higher order Fourier components in the magnetic field created by the helical coils.[21] Since the magnetic islands with different mode numbers overlap each other in the ergodic layer, the magnetic field structure becomes entirely three-dimensional. The magnetic field structure in the ergodic layer at a horizontally elongated plasma cross section ($\phi = 0°$) is shown in Figs. 1(b) and 1(c) for $R_{ax} = 3.75$ m and 3.90 m configurations, respectively. It indicates that the magnetic field connection length, L_c, in the ergodic layer varies within the extremely wide range of $10 \le L_c \le 2000$ m. In addition, two edge separatrix X-points appear at the inboard and outboard sides in the figure. In the present paper, those are called the "inboard edge X-point" and "outboard edge X-point." In contrast to this, the two positions close to the helical coil are called the "top edge O-point" and "bottom edge O-point." It is clear from the figures that the thickness of the ergodic layer, λ_{erg}, varies with the poloidal angle. The maximum and minimum thicknesses of the ergodic layer at the $\phi = 0°$ toroidal position, at which the LHD plasma cross section is horizontally elongated, are given at the edge X- and O-points, respectively. It is noted here that the plasma cross section periodically rotates as a function of the toroidal angle and becomes a vertical elongation at $\phi = 18°$ (see also Fig. 3). The magnetic field line called the "divertor leg" originating in the vicinity of the edge X-points is directly connected to the divertor plates made of graphite.

The magnetic field structure in the ergodic layer is very different between the two magnetic axis positions of $R_{ax} = 3.75$ m and 3.90 m. The LCFS becomes smaller when the magnetic axis position is shifted outward, whereas the outside boundary of the ergodic layer basically does not change at all. As a result, the λ_{erg} in the $R_{ax} = 3.90$ m configuration is much larger than that in the $R_{ax} = 3.75$ m configuration. The λ_{erg} has the biggest value in the inboard edge X-point of the horizontally elongated plasma cross section ($\phi = 0°$) at $R_{ax} = 3.90$ m configuration, i.e., $\lambda_{erg} \sim 60$ cm, while the magnetic field lines at the outboard edge X-point are dominantly connected to the divertor plates, as seen in Fig. 1(c). Many magnetic field lines with shorter L_c ($12 \le L_c \le 25$ m) appeared in the vicinity of the outboard X-point are connected to the divertor plates through the divertor legs in the $R_{ax} = 3.90$ m configuration.[22]

Ten pairs of normal conducting coils are additionally installed at the top and the bottom on the LHD as shown in Fig. 1(a) to create a considerably large magnetic island with the m/n = 1/1 mode in the plasma edge, which are now called resonant magnetic perturbation (RMP) coils. The RMP coil system was originally used for the local island divertor experiment to demonstrate an efficient particle exhaust.[15] As the island size can be controlled by the coil current, the maximum RMP coil current of $I_{coil} = 3340$ A is used in the present study to trigger the plasma detachment by creating the biggest island size. The edge magnetic field structure with the m/n = 1/1 island is then kept constant during the discharge by presetting the coil current.

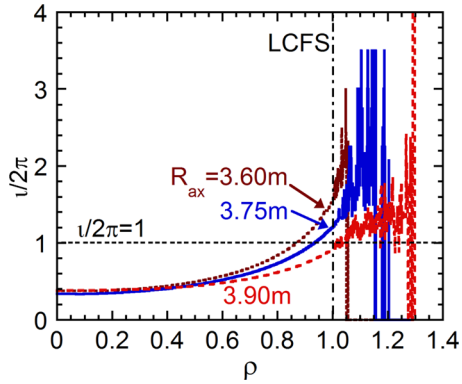


FIG. 2. $\iota/2\pi$ profile as a function of minor radius ($\rho \equiv r/a$) for $R_{ax} = 3.60$ m, 3.75 m, and 3.90 m. The "a" is averaged-plasma radius. The LCFS position is indicated by a dashed-dotted line.

Radial profiles of the rotational transform ($\iota/2\pi$) in LHD are shown in Fig. 2 as a function of minor radius ($\rho \equiv r/a$) for magnetic axis positions of $R_{ax} = 3.60$ m, 3.75 m, and 3.90 m. The $\iota/2\pi$ profile becomes gradually flat when the magnetic axis shifts outward. According to the change, the radial position of $\iota/2\pi = 1$ also moves outside, i.e., $\rho = 0.93$ inside LCFS ($\rho = 1$) at $R_{ax} = 3.75$ m and $\rho = 1.03$ just inside the ergodic

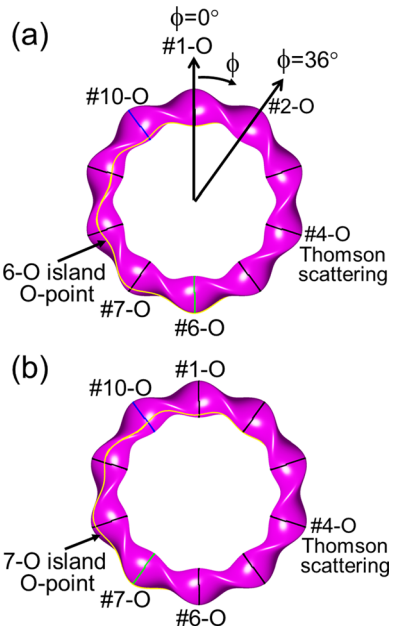


FIG. 3. Schematic view of the O-point trajectory of the m/n = 1/1 magnetic island on a flux surface at $\iota/2\pi = 1$ for (a) 6-O and (b) 7-O islands in $R_{ax} = 3.75$ m configuration.

layer at $R_{ax} = 3.90$ m. In the case of $R_{ax} = 3.90$ m, then, any clear magnetic island formation has not been observed in general discharges because the RMP field has in principle no clear magnetic resonance of the m/n = 1/1 mode in the stochastic magnetic field layer, while a considerably large island has been always formed by the RMP field in the $R_{ax} = 3.60$ and 3.75 m configurations. It is described below in detail.

Figure 3 shows the top view of the LHD plasma. The poloidal position of the m/n = 1/1 island can be slightly changed by phasing the RMP coil currents. The poloidal position of the island O-point is also indicated in the figures. The trajectory of the island O-point formed in the midplane at #6-O ($\phi = 180°$) and #7-O ($\phi = 216°$) outboard diagnostic ports is plotted with solid curves in Figs. 3(a) and 3(b), respectively. Here, we define the two configurations as "6-O island" and "7-O island." In practice, the trajectory of the island O-point in Fig. 3 is traced on a flux surface with $\iota/2\pi = 1$ at $R_{ax} = 3.75$ m configuration. The island O-point is then located for both the 6-O and 7-O island configurations in the inboard side of the horizontally elongated plasma cross section at the #10-O ($\phi = 326°$) diagnostic port where the spectrometers are installed, while the poloidal angle of the island O-point is slightly different between the two.

The poloidal structure of the magnetic island created by the RMP coils is generally calculated in the vacuum condition for the core plasma inside the LCFS. If the island exists in the ergodic layer, the structure can be obtained by tracing the 3-dimensional trajectory of each magnetic field line. The Poincaré plot of magnetic field lines without RMP coils in the ergodic layer is shown in Figs. 4(a) and 4(d) with magnetic surfaces for $R_{ax} = 3.75$ m and 3.90 m, respectively. Several intrinsically existing small magnetic islands appear in the ergodic layer, while well-arranged magnetic surfaces are seen in the plasma core region. The island structure with the RMP field at $R_{ax} = 3.75$ m is plotted in Figs. 4(b) and 4(c) for 6-O and 7-O island cases, respectively. Since the island exists inside the LCFS denoted as a dashed line, the magnetic field structure in the ergodic layer is not traced in the figures because it is nearly the same as in Fig. 4(a). The island with the m/n = 1/1 mode is localized at the inboard side of the #10-O toroidal position although the poloidal position of the island is a little different between 6-O and 7-O configurations. In the case of $R_{ax} = 3.90$ m, on the other hand, the island structure becomes much different from the $R_{ax} = 3.75$ m case because the $\iota/2\pi = 1$ position is located in the ergodic layer. The magnetic field lines at $R_{ax} = 3.90$ m configuration with RMP coils are plotted in Figs. 4(e) and 4(f) for 6-O and 7-O islands, respectively. In order to make clear the island position, the number of mesh in the calculation is increased compared with Figs. 4(a) and 4(d). It is then noted that the magnetic field structure in the plasma core is not plotted in Figs. 4(e) and 4(f) because the plasma core is entirely black if it is plotted in the figure. A small island can be seen in the ergodic layer just outside the LCFS of the figures, while the poloidal shape is entirely different from the ordinary island seen in the plasma core. In the present study, a poloidal position opposite to the island O-point is called the "island X-point" although the island X-point is not clearly visible in the Poincaré plot.

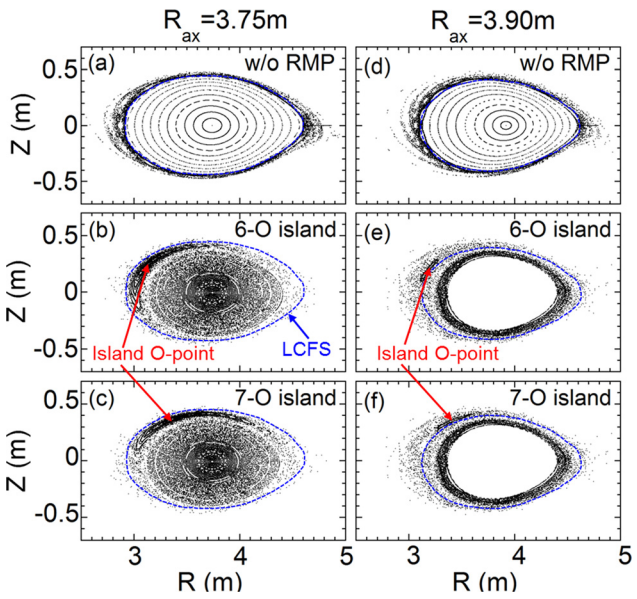


FIG. 4. Magnetic field structures in vacuum conditions at the #10-O toroidal location: (a) without RMP, (b) 6-O island and (c) 7-O island at $R_{ax} = 3.75$ m, and (d) without RMP, (e) 6-O island and (f) 7-O island at $R_{ax} = 3.90$ m. The LCFS in vacuum conditions without RMP is indicated by a dashed line in each figure.

III. EUV SPECTROSCOPY AND VUV SPECTROSCOPY IN LHD

The EUV and VUV spectrometer systems are installed on the #10-O LHD port ($\phi = 324°$ in Fig. 3). In the present study, two EUV spectrometers named EUV_Short (10–100 Å) and EUV_Long (50–650 Å) and two 20 cm normal incidence VUV spectrometers named VUV_109L (300−1000 Å) and VUV_106R (970−1900 Å) are used for simultaneous measurement of carbon spectra with a high-time resolution of 5 ms.[23–25] Two other space-resolved EUV spectrometers named EUV_Short2 (10–100 Å) and EUV_Long2 (50–650 Å) observe the vertical profile and 2-D distribution of carbon line emissions, respectively.[16–18,26] The intensities of EUV and VUV spectra are absolutely calibrated with sufficient accuracy on the basis of profile measurements of the bremsstrahlung continua in the visible and EUV ranges.[18,27]

The EUV_Long2 spectrometer is developed to observe both the vertical profile and the 2-D distribution of impurity line emissions.[17,18,22] As shown in Fig. 5(a), the spectrometer optical axis can be horizontally scanned around a pivot using a horizontal stepping motor. When the optical axis of the spectrometer is fixed perpendicular to the magnetic axis, i.e., $\theta = 0°$, the vertical profile of impurity emissions can be measured in the vertical observation range of $-600 \le Z \le 600$ mm at the horizontally elongated plasma cross section as shown in Figs. 1(b) and 1(c). The 2-D distribution of impurity emissions can be measured by horizontally scanning the optical axis from $\theta = -2°$ to $+2°$ during the steady phase of a discharge (see top three figures in Fig. 5(a)). As shown in Fig. 5(b), a large trapezoidal diagnostic port with a vertical size of 1200 mm and a horizontal size of 700 mm is used for the 2-D distribution measurement. Therefore, the impurity emissions

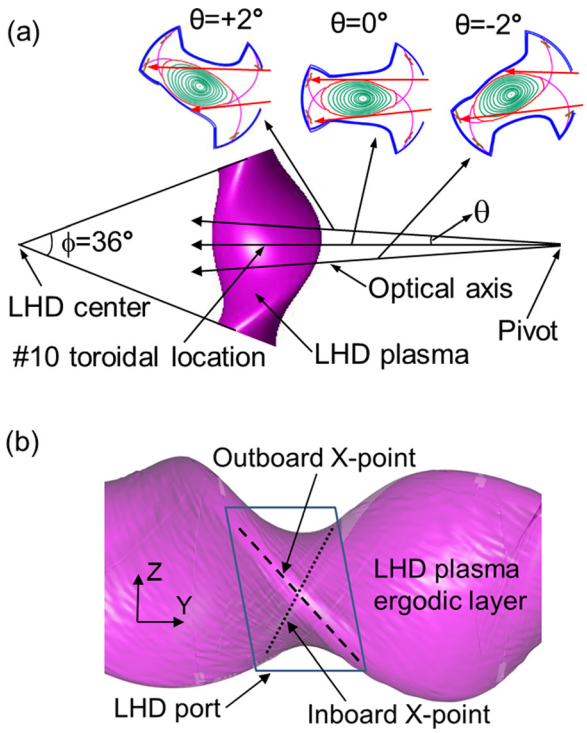


FIG. 5. (a) Top and (b) horizontal views of the LHD plasma shape with the observation area of the EUV_Long2 spectrometer system at the #10-O toroidal location. Three poloidal cross sections of the LHD plasma are also shown for three different angles in the spectrometer optical axis of $\theta = +2°$, 0°, and $-2°$. The top and bottom boundaries of the vertical observation range are indicated by two arrows in each poloidal cross section. The #10-O LHD diamond port for the 2-D distribution measurement is indicated by a solid line. Inboard and outboard X-point trajectories are indicated by dotted and dashed lines, respectively.

from inboard and outboard edge X-points can be clearly distinguished in the 2-D distribution measurement, as indicated in Fig. 5(b) with dotted and dashed lines, respectively.

The m/n = 1/1 island twists along the flux surface of $\iota/2\pi = 1$ during a toroidal turn (see Fig. 3). The vertical position of island O- and X-points then changes as a function of the horizontal position, Y, in the 2-D observation range, which is denoted as solid lines with the trapezoidal shape in Fig. 5(b). The footprints of the island O- and X-points in the 2-D observation range are shown in Figs. 6(a) and 6(c) for the 6-O island and in Figs. 6(b) and 6(d) for the 7-O island. The vertical location of $\iota/2\pi = 1$ is also indicated by dashed lines in each figure. There is a larger separation of the O- and X-points at the measurement position for the 6-O island case than for the 7-O island case independent of the magnetic axis position. The small differences in the island position between the $R_{ax} = 3.75$ and 3.90 m cases are caused by differences in the edge rotation transform shown in Fig. 2.

IV. IMPURITY CARBON EMISSIONS AT $R_{ax} = 3.75$ m CONFIGURATION WITH THE m/n = 1/1 ISLAND INSIDE LCFS

Carbon and iron ions always exist in LHD discharges as the intrinsic impurity, which originate in the graphite divertor tiles and stainless steel first wall, respectively. The amount of iron contamination is, however, entirely small in

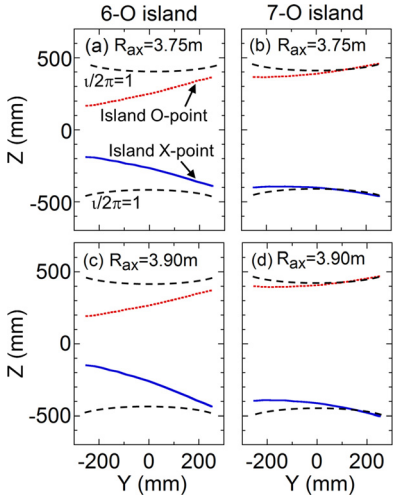


FIG. 6. Vertical positions of the O-point (dotted line) and X-point (solid line) of the m/n = 1/1 magnetic island within the observation area of the EUV_Long2 spectrometer installed on the #10-O LHD port: (a) 6-O and (b) 7-O islands at $R_{ax} = 3.75$ m configuration and (c) 6-O and (d) 7-O islands at $R_{ax} = 3.90$ m configuration. The radial location of $\iota/2\pi = 1$ is also indicated by a dashed line in each figure.

most of the LHD discharges due to the presence of the screening effect in the ergodic layer.[15] Although the iron radiation from highly ionized iron can be significant in the plasma core, it can be ignored in the analysis of the edge plasma including the ergodic layer because the line emissions from lower charge states of iron are negligibly small in both the VUV and the EUV wavelength ranges. Therefore, the carbon ions are largely responsible for the edge radiation in LHD discharges. Line emissions of CIII–CVI are then studied in discharges at $R_{ax} = 3.75$ m and 3.90 m since the m/n = 1/1 island in inward-shifted magnetic axis positions such as $R_{ax} = 3.60$ m is located deep inside the plasma radius. As the first step in the study, therefore, the vertical profile and 2-D distribution of CIII–CVI are analyzed in discharges at $R_{ax} = 3.75$ m.

A. Discharge waveform and radial profiles of n_e and T_e

A discharge initiated by electron cyclotron heating (ECH) in $R_{ax} = 3.75$ m configuration can be steadily maintained with negative-ion-source-based NBIs (n-NBI) at the toroidal magnetic field of $B_t = -2.64$ T, where the minus sign indicates a counter-clockwise directed toroidal field. The waveform of typical discharges with and without RMP is shown in Fig. 7. A constant line-averaged electron density (n_e) is kept during t = 4–8 s by controlling the hydrogen gas puff rate, while the density in the discharge with RMP is slightly smaller than that without RMP, i.e., $n_e = 4.0$ and 4.5×10^{13} cm^{-3} for the discharge with and without RMP, respectively. The central electron temperature (T_{e0}) also shows a constant value around 1.8 keV during t = 4–8 s for both discharges. The diamagnetic plasma stored energy (W_p) in the discharge with RMP is significantly lower than that in the discharge without RMP reflecting the edge temperature reduction as seen in Fig. 8(b). The radiation loss power (P_{rad}) in the discharge with RMP also indicates a lower value compared to that without RMP, mainly reflecting the steep edge

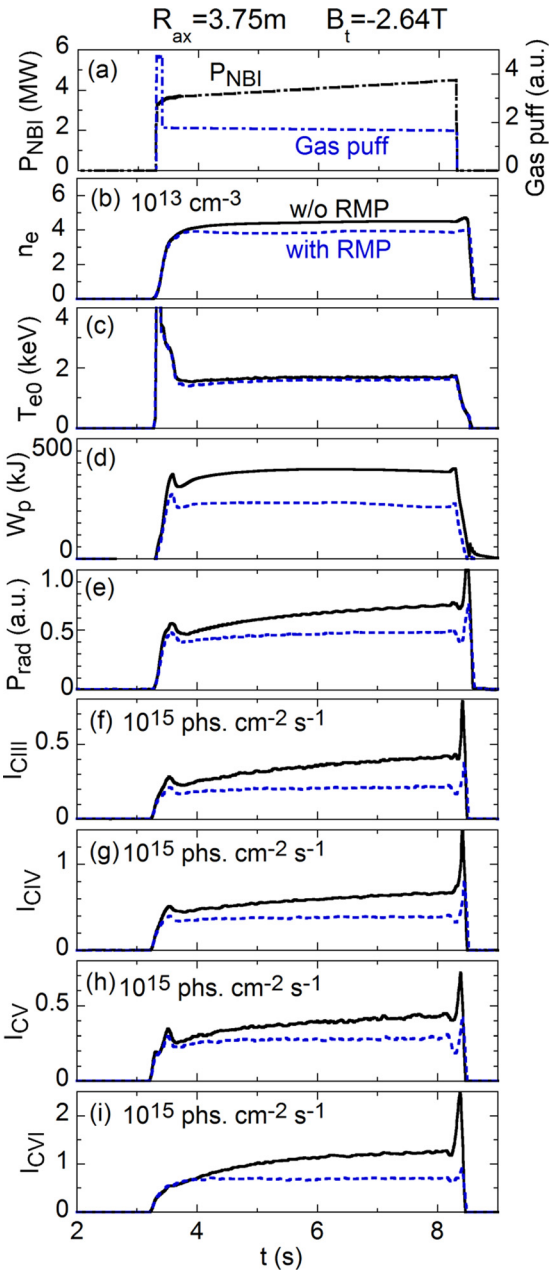


FIG. 7. Time behaviors of (a) NBI port-through power and hydrogen gas puff (b) line-averaged electron density, (c) central electron temperature, (d) stored energy, (e) radiation loss power, (f) CIII (386.203 Å), (g) CIV (384.174 Å), (h) CV (40.27 Å), and (i) CVI (33.73 Å) in #130913 and #130914 discharges at $R_{ax} = 3.75$ m without (solid line) and with RMP (dashed line).

temperature gradient as seen in Fig. 8(b). The reduction in edge radiation is also observed in carbon line emissions of CIII (386.203 Å), CIV (384.174 Å), CV (40.27 Å), and CVI (33.73 Å) plotted in Figs. 7(f), 7(g), 7(h), and 7(i), respectively.

The radial profiles of n_e and T_e measured with the Thomson scattering diagnostic along the major radius direction in the horizontally elongated plasma cross section at #4-O ($\phi = 144°$) are shown in Fig. 8 for discharges without (open circles) and with RMP (6-O island: solid circles and 7-O island: solid squares). A hollow density profile is always observed in the discharges without RMP. The density profile

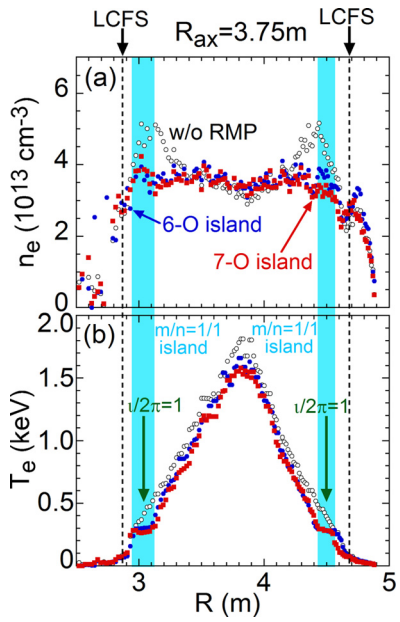


FIG. 8. Radial profiles of (a) n_e and (b) T_e in discharges at $R_{ax} = 3.75$ m without RMP (open circles), with 6-O island (solid circles), and with 7-O island (solid squares). Radial locations of LCFS and $\iota/2\pi = 1$ are indicated by dashed lines and vertical arrows, respectively. The radial range of the m/n = 1/1 island is indicated by a shaded area.

becomes flat when the RMP is supplied. The m/n = 1/1 magnetic island is clearly identified at the $\iota/2\pi = 1$ position indicated by vertical arrows inside the LCFS. The LCFS and the radial width of the m/n = 1/1 island are denoted as a dashed line and shaded area, respectively. Since the #4-O toroidal port is away from the #6-O and #7-O ports by $\phi = 72°$ and 108°, respectively, the edge T_e flattening can be observed at both the inboard and the outboard sides (see Fig. 3). The shape of T_e flattening is slightly different between the 6-O and 7-O islands, reflecting a small difference in the poloidal angle of the island. Since the temperature in the island is in the range of $250 \leq T_e \leq 300$ eV, which is much higher than the ionization energies of C^{2+} (48 eV) and C^{3+} (64 eV) ions, the radiation from such ions exists in the ergodic layer outside the LCFS entirely and has no relation to the appearance of the island. The T_e in the plasma core region is reduced by the edge T_e reduction following the edge T_e flattening, whereas the T_e outside the LCFS is almost unchanged.

B. EMC3-EIRENE code for the analyses of 3-D impurity distribution and cross-field impurity transport

The 3-D distributions of the carbon ion density and resultant line emissions of CIII (386.203 Å), CIV (312.42 Å), CV (40.27 Å), and CVI (33.73 Å) are simulated with a 3-D edge plasma transport code, EMC3-EIRENE. The EMC3 code for solving the fluid equations of the particle, momentum, and energy in the steady state is coupled with the EIRENE code for solving the kinetic neutral transport equations coupled with the recycling neutrals from divertor plates and the first wall.[28,29] The EMC3 modelling includes parallel and cross-field transports in a 3-D geometry of the magnetic field. The transport of the bulk plasma and impurity along the magnetic field line is considered to be classical, while the

cross-field transport perpendicular to the magnetic field line is assumed to be anomalous.[28]

In the fluid approximation, the momentum balance equation of impurity ions along the magnetic field line is given by

$$m_z \frac{\partial V_{z\|}}{\partial t} = -\frac{1}{n_z}\frac{\partial T_i n_z}{\partial s} + m_z \frac{V_{i\|} - V_{z\|}}{\tau_{zi}} + ZeE_{\|} + 0.76Z^2 \frac{\partial T_e}{\partial s} + 2.6Z^2 \frac{\partial T_i}{\partial s}, \quad (1)$$

where z and i denote the impurity with charge state Z and the bulk plasma ion, respectively. The notation s is the coordinate along the magnetic field line. The variables $V_{i||}$, $V_{z||}$, τ_s, m_z, and $E_{||}$ denote the parallel velocities of the bulk plasma and impurity, impurity-ion collision time, impurity ion mass, and parallel electric field, respectively. The values of T_z and T_i denote the temperatures of the impurity and the bulk plasma ions, respectively, and $T_z = T_i$ is assumed in the equation. The inertia term shown in the left-hand side of the equation can be neglected due to a small value.[15] The first term on the right-hand side of the equation shows the impurity pressure gradient force. The second and third terms are the force due to the friction between the impurity and bulk plasma ions and the force due to the parallel electric field, respectively. The fourth and fifth terms on the right-hand side are the forces due to the electron and ion temperature gradients, respectively. It has been proven that the second and fifth terms in the right-hand side are dominant in the equation. This means that the friction force and the ion thermal force become dominant in the force balance on the parallel impurity transport for the usual plasma parameters. The flow of the bulk plasma ions, $V_{i||}$, is usually directed towards the downstream, i.e., from the plasma edge to the divertor plates, and the friction force moves the impurity ions to the divertor region. On the other hand, the temperature gradient, $\partial T_i/\partial s$, is directed towards the upstream, i.e., from the divertor plates to the plasma edge, and the thermal force moves the impurity ions to the upstream direction. Therefore, the impurity velocity, $V_{z||}$, is a consequence of the competition between the friction and the ion thermal forces. If the friction force is more dominant than the thermal force, the impurity ions can be screened.

The cross-field transport is also important in the ergodic layer of LHD where the connection length of magnetic field lines is very long. In the EMC3 code, the cross-field transport of bulk and impurity ions is assumed to be anomalous. Here, it is noted that the bulk ions in LHD are protons. The particle diffusion coefficient, $D_\perp$, and heat conduction coefficient, $\chi_\perp$, are determined for bulk plasmas by analyzing the edge density and temperature profiles measured with Thomson scattering diagnostic. Spatially constant values of $D_\perp$ and $\chi_\perp$ are used in the code. Although the cross-field impurity diffusion of impurity ions, $D_{Z\perp}$, may be different from that of the bulk ions,[30,31] the impurity motion in the present modeling is simply smoothed out towards the perpendicular direction with $D_{Z\perp}$. The poloidal distribution of impurity line emissions is therefore more uniform when the $D_{Z\perp}$ is large. The $D_{Z\perp}$ different from $D_\perp$ is also used in the present analysis to reproduce the measured profile of impurity line emissions.

In the simulation for $R_{ax} = 3.75$ m configuration, $D_\perp = 0.2$ m^2/s and $\chi_\perp = 0.5$ m^2/s are chosen for the bulk plasmas based on the analysis of the edge electron density and temperature profiles shown in Fig. 8. The amount of impurity carbon is mainly dependent on the sputtering yield of the graphite divertor plates, C_{sput}. In the present study, the sputtering rate of $C_{sput} = 0.5\%$ has been used for the graphite divertor plate.[30,31] Figure 9 shows the simulated 2-D distribution of CIII–CVI emissivity in the ergodic layer at the horizontally elongated plasma cross section. It is clear that the CIII and CIV with low ionization energies, i.e., 48 eV for C^{2+} and 64 eV for C^{3+}, are mainly located near the outer boundary of the ergodic layer or in the vicinity of divertor legs, while the CV and CVI are located inside the ergodic layer due to the high ionization energies, i.e., 392 eV for C^{4+} and 490 eV for C^{5+}.[32] Therefore, the poloidal distributions of CIII and CIV are entirely non-uniform with enhanced intensity in the vicinity of the inner and outer X-points, whereas the CV and CVI intensities show a more uniform poloidal distribution. Since it is difficult to calculate the impurity emissions inside the LCFS using the EMC3-

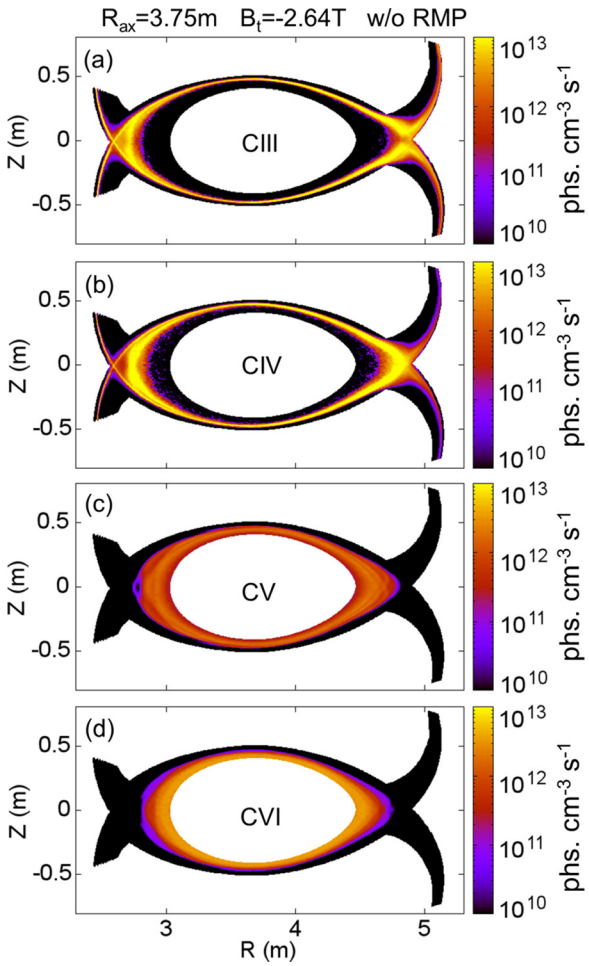


FIG. 9. Poloidal distributions of impurity emissivity in the ergodic layer calculated with EMC3-EIRENE for (a) CIII (386.203 Å), (b) CIV (312.42 Å), (c) CV (40.27 Å), and (d) CVI (33.73 Å) in discharges without RMP at $R_{ax} = 3.75$ m.

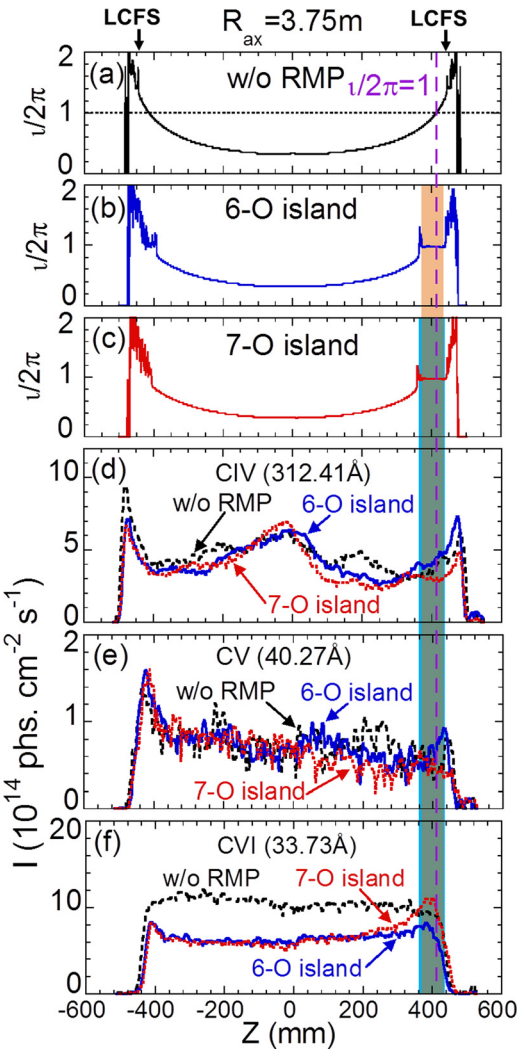


FIG. 10. $\iota/2\pi$ profiles (a) without RMP, (b) with 6-O island, and (c) with 7-O island and vertical profiles of (d) CIV (312.42 Å), (e) CV (40.27 Å), and (f) CVI (33.73 Å) at the #10-O toroidal location in discharges at $R_{ax} = 3.75$ m without RMP (dashed line), with 6-O island (solid line), and with 7-O island (dotted line). Radial locations of LCFS and $\iota/2\pi = 1$ are indicated by vertical arrows and dashed line, respectively. The radial distributions of the m/n = 1/1 island are indicated by shaded areas with different colors for the 6-O (brown) and 7-O island (sky blue).

EIRENE code, the CVI emission inside the LCFS is not plotted in Fig. 9(d) due to the absence of data. In addition, no up-down asymmetry is observed in the simulation results at $\phi = 0°$ because the magnetic field structure in the ergodic layer is basically identical between the upper and lower edge regions.

C. Vertical profiles of carbon line emissions

The vertical profile of CIV to CVI is measured at t = 6.0 s during the density and temperature flat-top phase shown in Fig. 7 for three configurations, i.e., without RMP, 6-O island, and 7-O island. The results are plotted in Figs. 10(d), 10(e), and 10(f) for CIV, CV, and CVI, respectively. The $\iota/2\pi$ profiles for the three configurations are also plotted in Figs. 10(a), 10(b), and 10(c). The positions of LCFS and island O-point are indicated by vertical arrows at the top of figures and as a vertical dashed line, respectively. Since the island O-point is located in the upper position at the #10-O toroidal section for both the 6-O and 7-O islands (see Figs. 4(b) and 4(c)), the local flattening of $\iota/2\pi$ appears at the top of the vertical profile. The radial range of the m/n = 1/1 island is denoted by a shaded area. The radial width of the m/n = 1/1 island is roughly 8 cm at the top edge O-point as seen in Figs. 10(b) and 10(c). When the island O-point is located at the edge X-point, the radial width becomes bigger as seen in the T_e profile of Fig. 8(b).

In general discharges without RMP, the CIV profile is poloidally non-uniform and vertically asymmetric as shown in Fig. 10(d). In contrast to this, the CVI profile is roughly symmetric as shown in Fig. 10(e). The edge peaks in CIV at $Z \sim \pm 500$ mm and CV at $Z \sim \pm 440$ mm are formed by a long integration effect along the observation chord in the thin CIV and CV emission contours (see Figs. 9(b) and 9(c)). In addition, the CIV is also enhanced in the range of $-300 \leq Z \leq 300$ mm in the vicinity of inboard and outboard edge X-points, while the CV and CVI profiles seem to be flat. This can be well explained by the simulation (see Fig. 9). The big volume of the ergodic layer near the separatrix X-point causes the enhancement of the CIV emission. The emission from upper half at $-500 \leq Z \leq 0$ mm tends to have a greater intensity compared with the emission from lower half at $0 \leq Z \leq 500$ mm. In particular, this is clear in the CIV and CV profiles, suggesting an up-down asymmetry in the edge impurity radiation.

When the RMP is supplied, the CIV and CV profiles do not make any big change in the upper half structure because the T_e and n_e profiles are unchanged in the ergodic layer outside the LCFS (see Fig. 8). Therefore, the m/n = 1/1 island has little influence on the CIV and CV profiles in the $R_{ax} = 3.75$ m configuration. On the other hand, the CVI profile in Fig. 10(f) indicates a significant change when the RMP is supplied. The CVI intensity is clearly reduced for both the 6-O and 7-O island cases. With the RMP, the impurities intrinsically existing in LHD plasmas such as carbon

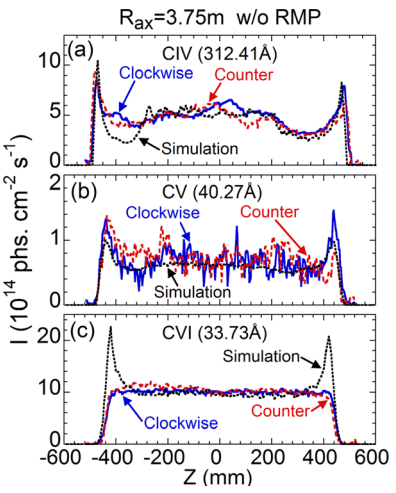


FIG. 11. Vertical profiles of (a) CIV (312.42 Å), (b) CV (40.27 Å), and (c) CVI (33.73 Å) measured at the #10-O toroidal location in discharges at $R_{ax} = 3.75$ m with a toroidal magnetic field in clockwise ($B_t = 2.64$ T: solid line) and counter-clockwise ($B_t = -2.64$ T: dashed line) directions and simulated with EMC3-EIRENE (dotted line).

and iron are always decreased in the plasma core despite the unchanged influx. The enhanced edge impurity screening is the reason why the CVI intensity decreases.[19] It is also noticed that the CVI intensity increases at the top O-point near $Z = 400$ mm where the island O-point exists. This seems to be an effect of edge temperature flattening shown in Fig. 8(b). Here, it is concluded that the $m/n = 1/1$ island at $R_{ax} = 3.75$ m configuration changes only the CVI distribution located near the island, and the effect of the $m/n = 1/1$ island on the CIV and CV distributions is small.

The up-down asymmetry is slightly enhanced when the B_t is in the counter-clock wise direction, e.g., $B_t = -2.64$ T.[15] A comparison between CIV−CVI vertical profiles is shown in Fig. 11 for clockwise (solid lines) and counter-clockwise (dashed lines) B_t directions. It is clear that the up-down asymmetry is emphasized in the case of the counter-clockwise direction, in particular, for CV. Although the physical mechanism is unclear at present, this asymmetry may suggest an importance of the particle drift. Since the edge peak position indicates the radial location of carbon ions, we understand that both C^{3+} and C^{4+} ions are located outside the $\iota/2\pi = 1$ position and the C^{5+} ions are located very close to the $\iota/2\pi = 1$ position.

The CIV−CVI vertical profiles are also analyzed with EMC3-EIRENE, as plotted a dotted line in Fig. 11. The intensity profiles are normalized to the measurement at $Z = 0$ mm. Since the EUV_Long2 spectrometer is placed at $R = 9300$ mm away from the LHD plasma and $Z = 463$ mm above the midplane, the observation chords are vertically inclined a little. Then, the simulation with experimental geometry does not exactly show the vertical symmetry. Although the effect of the inclined observation chord on the profile is very small, we see the effect in the simulation of the CIV profile at $Z \sim \pm 400$ mm because the CIV is emitted in the outer boundary of the ergodic layer. The simulation can well explain the CIV and CV profiles, in particular, in the clockwise B_t direction. In the counter-clockwise direction, however, a small difference appears in both the top and bottom edge regions. In the present simulation code, the effects of plasma pressure on the magnetic field structure in the ergodic layer and particle motion on the impurity transport such as ∇B drift are not included. These effects, in particular, the particle drift, may explain the up-down symmetry, while the direction of the particle drifts such as ∇B drift is not as simple as it in tokamaks. In the simulation, a cross-field impurity diffusion coefficient of $D_{Z\perp} = 1.0$ m^2/s, of which is five times larger than that of the bulk ions, is used for carbon ions to match the experiment.

In the CVI simulation, the emission inside the LCFS is not included in the emissivity profile because the code is not applicable to the core plasma with the magnetic surface. Therefore, the CVI edge peaks appeared at $Z = \pm 400$ mm near the edge O-point in the ergodic layer are unnecessarily enhanced. As the CVI emission near the edge X-point inside the LCFS is very strong, the real CVI profile becomes roughly flat as seen in the experiment. The CVI emissivity is also slightly stronger at the lower half of the plasma in the counter-clockwise B_t direction, while the profile in the clockwise direction is almost flat.

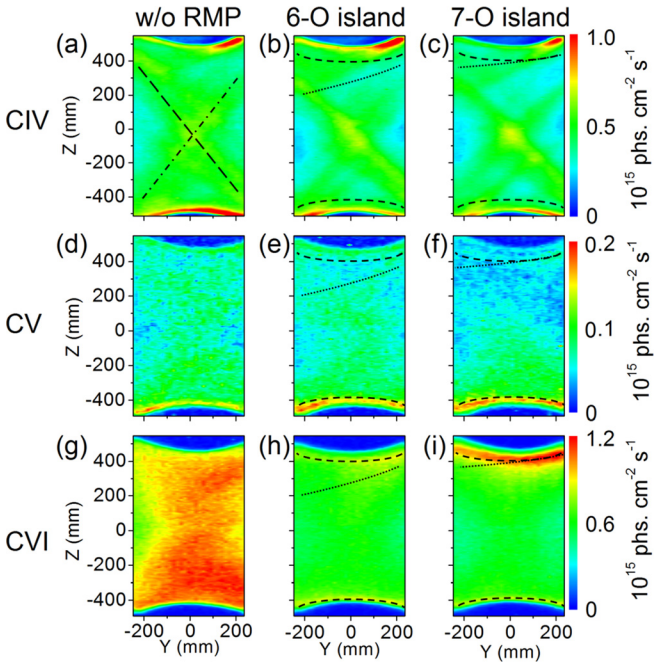


FIG. 12. 2-D distributions at $R_{ax} = 3.75$ m of CIV (312.42 Å) in discharges (a) without RMP, (b) with 6-O island, and (c) with 7-O island; CV (40.27 Å) in discharges (d) without RMP, (e) with 6-O island, and (f) with 7-O island; and CVI (33.73 Å) in discharges (g) without RMP and (h) with 6-O island. Trajectories of the outboard X-point, inboard X-point, and island O-point are indicated by long dashed, dotted-dashed, and dashed lines, respectively. The radial location of the $\iota/2\pi = 1$ profile is indicated by dashed lines in each figure.

D. 2-D distribution of carbon line emissions

In order to study the effect of the $m/n = 1/1$ island on the carbon emission in greater detail, the 2-D distribution of CIV−CVI at $R_{ax} = 3.75$ m is analyzed, as shown in Fig. 12.

In general discharges without RMP, the 2-D CIV distribution shown in Fig. 12(a) indicates that the emission is dominant at the top and bottom edges and in the vicinity of inboard and outboard X-points. The footprints of the inboard and outboard X-points are traced in Fig. 12(a) with dashed-dotted and long-dashed lines, respectively. The schematic view in Fig. 5(b) and the simulation in Fig. 9(b) are also helpful for understanding Fig. 12(a). In contrast to it, the CV and CVI distributions shown in Figs. 12(d) and 12(g) are almost uniform except for the bottom edge. The up-down asymmetry brought by the effect of the counter-clockwise toroidal magnetic field is also observed in the 2-D distributions of CIV−CVI.

The 2-D distribution of carbon emissions is also simulated with the EMC3-EIRENE code.[30,31] The 2-D plot of the CIV simulation shown in Fig. 13(a) indicates emission enhancements not only in the top and bottom edges but also along several footprints parallel to the inner and outer X-points. The simulated result in Fig. 13(a) with $D_{Z\perp} = 0.2$ m^2/s is considerably different from the experimental result in Fig. 12(a), while the intensity is in the same level. The CV simulation in Fig. 13(c) also indicates a different structure from the experiment in Fig. 12(d). A larger impurity diffusion coefficient is then adopted in the simulation to match the experimental data. The results with $D_{Z\perp} = 1.0$ m^2/s are

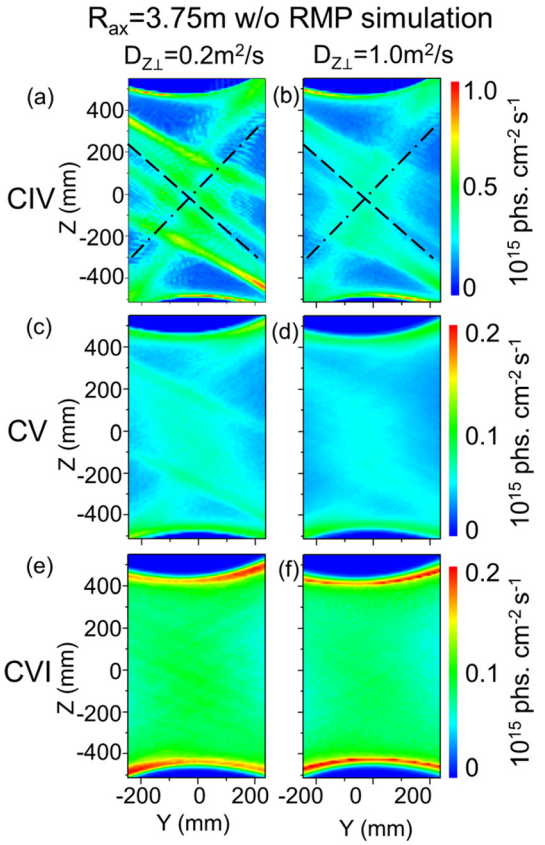


FIG. 13. 2-D emissivity distributions simulated with EMC3-EIRENE in $R_{ax} = 3.75$ m configuration without RMP for (a) CIV (312.42 Å), (c) CV (40.27 Å), and (e) CVI (33.73 Å) at an impurity diffusion coefficient of $D_{Z\perp} = 0.2$ m^2/s and (b) CIV, (d) CV, and (f) CVI at $D_{Z\perp} = 1.0$ m^2/s. Trajectories of outboard and inboard X-points are indicated by long dashed and dotted-dashed lines, respectively.

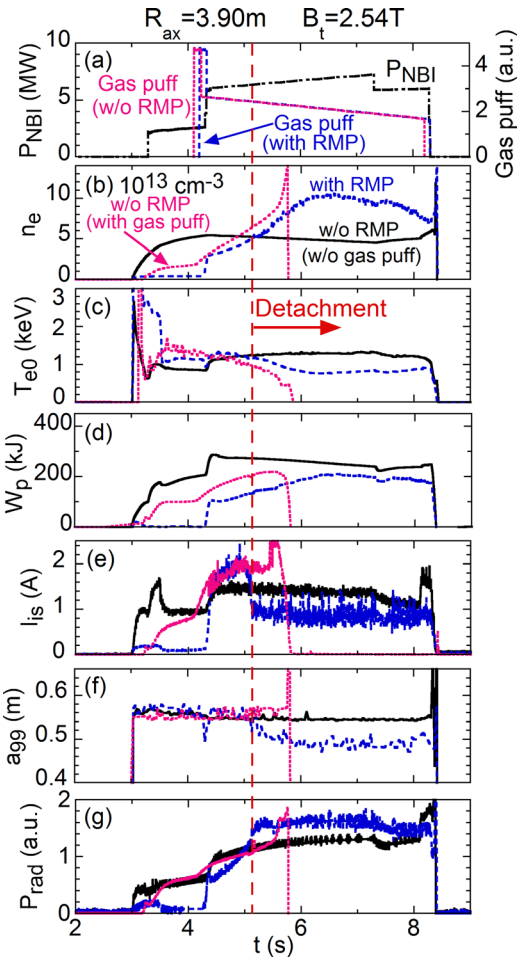


FIG. 14. Time behaviors of (a) NBI port-through power and gas puff, (b) line-averaged electron density, (c) central electron temperature, (d) stored energy, (e) ion saturated current, (f) effective plasma radius, and (g) radiation loss power in discharges at $R_{ax} = 3.90$ m without RMP (gas puff: solid line, no gas puff: dotted line) and with RMP (dashed line). The timing of detachment transition is indicated by a vertical dotted line.

shown in Figs. 13(b) and 13(d) for CIV and CV, respectively. The sharp footprints related to the edge X-points appeared in Figs. 13(a) and 13(c) almost disappear in Figs. 13(b) and 13(d). The simulated results with large $D_{Z\perp}$ are roughly in agreement with the experimental results in Figs. 12(a) and 12(d). However, there still remain unclear points, in particular, in the angle of X-point footprints between the simulation and experiment. In the simulation code, as mentioned above, a modification of the magnetic field structure in the ergodic layer based on the plasma pressure and the particle drift motion is not included. An improvement in the simulation code is necessary for further discussions. The 2-D simulation of CVI in Fig. 13(e) with intensity enhancement near the top and bottom indicates a clear difference from the experiment in Fig. 12(g). This difference is also caused by the absence of simulation results inside the LCFS, as well as the discrepancies shown in Fig. 11(c).

Even if the RMP is supplied, the CIV and CV distributions do not obviously change, as shown in Figs. 12(b), 12(c), 12(e), and 12(f), whereas a significant change is observed in the 2-D distribution of CVI, as shown in Figs. 12(h) and 12(j). In the 6-O island case shown in Fig. 12(h), the CVI is slightly enhanced at the top and bottom edges. In the 7-O island case shown in Fig. 12(i), however, the CVI is clearly strong at the top edge. The footprint of the island O-point is indicated in the figures with a dotted line and the radial location of $\iota/2\pi = 1$ is also indicated by a dashed line for both the 6-O and 7-O island cases. Then, we understand that the CVI intensity is basically enhanced in the vicinity of the island O-point seeing Figs. 4(c) and 12(i).

V. IMPURITY CARBON EMISSIONS AT $R_{ax} = 3.90$ m CONFIGURATION WITH THE m/n = 1/1 ISLAND OUTSIDE LCFS

A. Discharge waveform and radial profiles of n_e and T_e

Vertical profiles and 2-D distributions of CIII–CVI are also studied in the attached and detached plasmas for the $R_{ax} = 3.90$ m configuration. Figure 14 shows a typical waveform of NBI discharges without RMP (with gas puff: solid line, no gas puff: dotted line) and with RMP (dashed line) at $R_{ax} = 3.90$ m with $B_t = 2.54$ T. The discharge initiated by ECH at $t = 3.0$ s is maintained by n-NBIs during 5 s at $t = 3.3$–8.3 s. In the discharge without RMP, no gas feed is utilized to avoid the radiation collapse, which usually occurs during high density operation.[12] Once the gas feed is supplied to the discharge, the density continuously increases,

and finally, the discharge meets the plasma collapse by rapidly increased radiation loss as shown in Fig. 14. The radiation collapse is also probably related to a worse fueling rate based on the enhanced edge particle shielding by the presence of the thick ergodic layer in the $R_{ax} = 3.90$ m configuration. In the case with no fueling and no RMP, the line-averaged density and central electron temperature are roughly constant during 3.5 s from 4.5 to 8.0 s, i.e., $n_e \sim 5 \times 10^{13}\,cm^{-3}$ and $T_{e0} \sim 1.2$ keV. The 2-D carbon emission distribution is observed during the constant phase. The total ion saturation current, I_{is}, measured with the Langmuir probe array embedded in the divertor plates shown in Fig. 14(e) and the effective plasma radius denoted with a_{99} shown in Fig. 14(f) are constantly maintained at the values of $I_{is} = 1.2$ A and $r_{eff} = 0.55$ m during 3.5 s, indicating the unchanged edge plasma condition and plasma volume. Here, the value of a_{99} often used in LHD is defined by a plasma radius in which 99% of the total plasma energy is confined. The effective plasma radius is calculated based on the T_e and n_e profiles from the Thomson scattering diagnostic.

When the RMP is supplied, the discharge conditions drastically change to an entirely different state at a critical threshold density. As shown in Fig. 14(e), the ion saturated current suddenly decreases by 60% at t = 5.1 s denoted with a vertical dotted line at which the density reaches the threshold, and the current keeps a low value until the end of the discharge. This current behavior indicates a specific feature of the plasma detachment. In the present discharge, the density threshold is $n_e \sim 5 \times 10^{13}\,cm^{-3}$, while it slightly depends on the NBI input power. After the transition to the detachment plasma, the electron density continuously increases until t = 6.3 s and saturates at $n_e \sim 12 \times 10^{13}\,cm^{-3}$. The central electron temperature starts to decrease after the detachment transition due to the density increase and finally stays at $T_{e0} \sim 0.8$ keV. In contrast, the stored energy still continues to increase even after the detachment transition and takes a similar temporal behavior to the density. Another specific feature at the detachment transition appears in the effective plasma radius. The initial effective plasma radius of $r_{eff} = 0.55$ m starts to decrease after the detachment transition and reaches $r_{eff} = 0.48$ m. The plasma radius remains constant until the end of discharge. The radiation power is also increased and remains at a high level during the plasma detachment phase. It should be noted here that the absolute value of the total radiation power has not been yet obtained due to a calibration problem caused by the 3-D radiation structure. The time behaviors of carbon line emissions of CIII (386.203 Å), CIV (384.174 Å), CV (40.27 Å), and CVI (33.73 Å) are shown in Fig. 15. The CIII−CV emissions significantly increase during the detachment phase, indicating the enhancement of edge radiation. However, only the CVI emission during the detachment phase is clearly lower than that during the attached phase without RMP, whereas the density during the detachment phase is much higher. It strongly suggests an enhancement of the impurity screening effect brought by the additional RMP field.

The radial profiles of n_e and T_e measured at t = 7.0 s in Fig. 14 are shown in Fig. 16 for three different discharges, i.e., attached plasma without RMP (open circles), 6-O island with detachment (solid circles), and 7-O island with

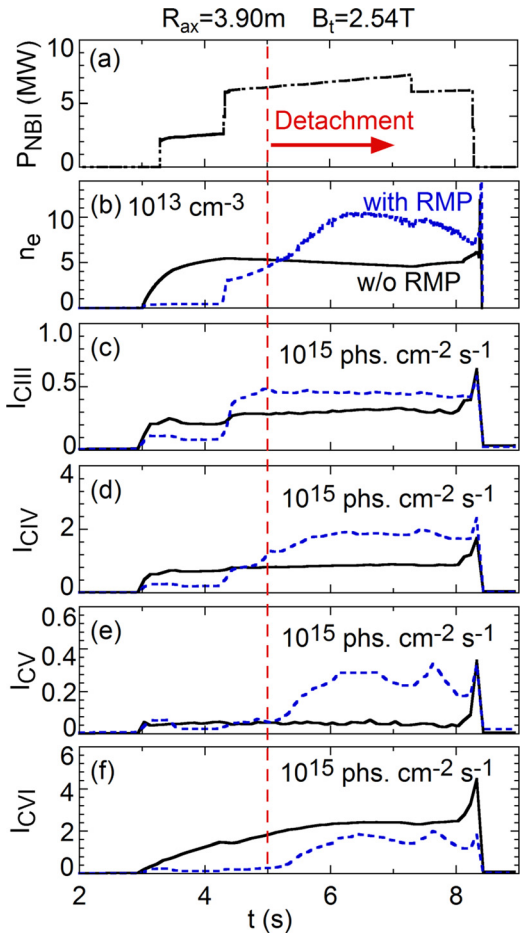


FIG. 15. Time behaviors of (a) NBI port-through power, (b) line-averaged electron density and intensities of (c) CIII (386.203 Å), (d) CIV (384.174 Å), (e) CV (40.27 Å), and (f) CVI (33.73 Å) in #128170 and #128189 discharges at $R_{ax} = 3.90$ m without (solid line) and with RMP (dashed line).

detachment (solid squares). The radial positions of $\iota/2\pi = 1$ and LCFS are denoted with vertical arrows and vertical dashed lines, respectively. The radial location of the m/n = 1/1 island is denoted by a shaded area. The density in the plasma core largely increases for both the 6-O and 7-O island cases after the detachment transition, of which the densities are a few times larger than the density in the attached plasma without RMP. On the other hand, the temperature in the plasma core at the detachment phase is much lower than that in the discharge without RMP.

It is very interesting to examine the effect of the island in the density and temperature profiles. One of the specific features is observed in the edge density profile, that is, the density starts to build up in the vicinity of the island, while the density also increases outside the island location. This phenomenon also appears in the density profile at $R_{ax} = 3.75$ m configuration shown in Fig. 8(a). The effect of the island also appears in the edge temperature profile. Figure 16(c) shows an enlarged T_e profile in the edge region. An edge temperature flattening is clearly seen near the island position, and the flat temperature ranges in $10 \le T_e \le 20$ eV. The C^{2+} and C^{3+} ions stay in the flat T_e region. The temperature profile at the 6-O island is slightly broadened compared with the profile at the 7-O island. This seems to be due to a difference in the

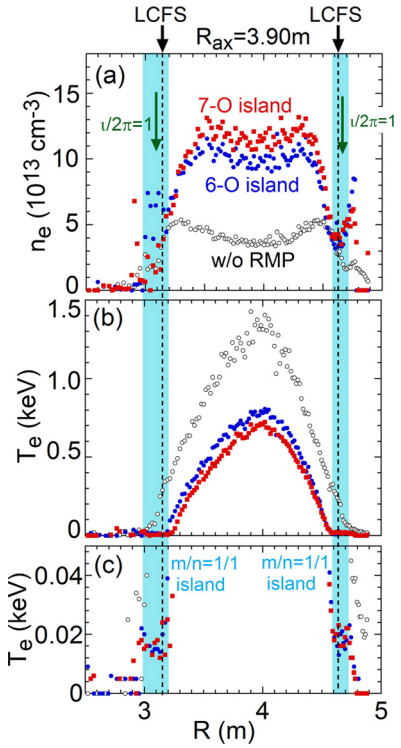


FIG. 16. Radial profiles of (a) n_e, (b) T_e, and (c) enlarged T_e in discharges at $R_{ax} = 3.90$ m without RMP (open circles), with 6-O island (solid circles), and with 7-O island (solid squares). Radial locations of LCFS and $\iota/2\pi = 1$ are indicated by dashed lines and vertical arrows, respectively. The radial range of the m/n = 1/1 island is denoted by a shaded area.

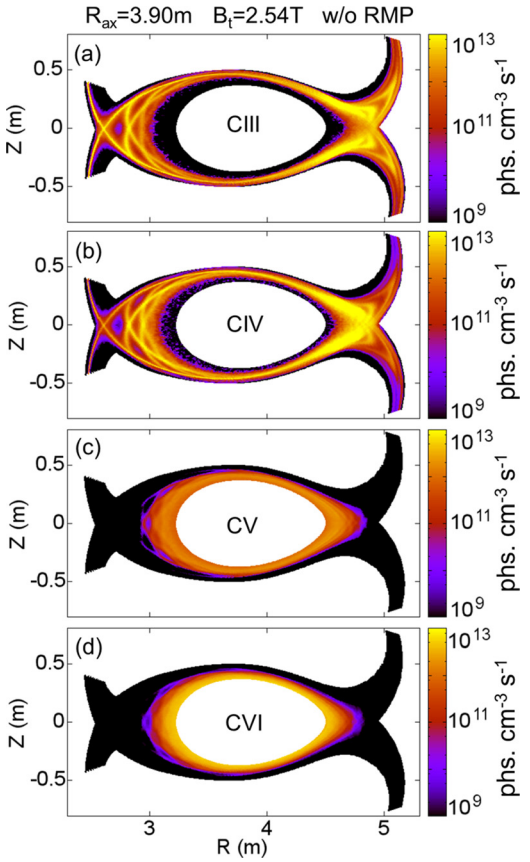


FIG. 17. Poloidal distributions of impurity emissivity in the ergodic layer simulated with EMC3-EIRENE for (a) CIII (386.203 Å), (b) CIV (384.174 Å), (c) CV (40.27 Å), and (d) CVI (33.73 Å) in $R_{ax} = 3.90$ m configuration without RMP.

deformation of the magnetic surface based on the plasma pressure effect.

B. Vertical profiles of carbon line emissions

The emissivity distribution of CIII−VI is simulated for $R_{ax} = 3.90$ m discharges and $R_{ax} = 3.75$ m case. The $D_\perp$ and $\chi_\perp$ are also determined by analyzing the edge electron density and temperature profiles shown in Fig. 16, i.e., $D_\perp = 0.2$ m^2/s and $\chi_\perp = 0.6$ m^2/s. The impurity diffusion coefficient of $D_{Z\perp} = 4.0$ m^2/s is used for carbon ions at all charge states in $R_{ax} = 3.90$ m. The reason is described below. The simulated result at $R_{ax} = 3.90$ m shown in Fig. 17 is closely similar to the previous result at $R_{ax} = 3.75$ m in Fig. 9, that is, the non-uniform CIII and CIV emissions are located near the outer boundary in the ergodic layer and the uniform CV and CVI emissions are located in the vicinity of LCFS. The 2-D plot of CIII and CIV emissivity shown in Figs. 17(a) and 17(b) indicates a complicated emission structure in the vicinity of inboard and outboard edge X-points. It reflects an entire 3-D magnetic field structure enhanced at $R_{ax} = 3.90$ m configuration. Comparing Figs. 17(a) and 17(b) with Fig. 1(c), it is clear that the CIII and CIV emissions are enhanced in the region where the connection length is in the range of $50 \le L_c \le 250$ m. Since the magnetic field lines in $R_{ax} = 3.90$ m configuration are dominantly connected to the divertor plates through the outboard X-point, the CIII and CIV emissions are stronger at the outboard X-point [see Fig. 1(c)].

The vertical profiles of $\iota/2\pi$ and CIII−CVI at $R_{ax} = 3.90$ m are shown in Fig. 18 for the attached plasma without RMP and the detached plasmas with 6-O and 7-O islands. The CIII−CVI profiles at t = 7.0 s in Fig. 14 are plotted in Figs. 18(d)–18(g). The radial position of $\iota/2\pi = 1$ indicated by a dashed line is located just outside the LCFS denoted by vertical arrows. A local flattening of the $\iota/2\pi$ profile appearing near the $\iota/2\pi = 1$ position is still visible for both the 6-O and 7-O islands in Figs. 18(b) and 18(c), respectively. The radial location of the $\iota/2\pi$ profile flattening is also indicated by a shaded area.

Since the ergodic layer outside LCFS is thick in $R_{ax} = 3.90$ m configuration, the plasma volume with lower temperatures becomes large. The CIII emission can be then measured with sufficient intensity in $R_{ax} = 3.90$ m as shown in Fig. 16(d), while the CIV−VI emissions are always strong as shown in Figs. 18(e)–18(g). The vertical profiles of CIII−CV in the attached plasmas without RMP denoted as dashed lines have a clear peak near the top and bottom edges, as well as the result of $R_{ax} = 3.75$ m, while the CVI in Fig. 18(g) has no such a peak. The CIII and CIV profiles also have an enhanced intensity in the vicinity of inboard or outboard X-points at $-300 \le Z \le 300$ mm. The up-down asymmetry is not observed for the profiles of CV and CVI. It may be the result of the clockwise magnetic field direction, i.e., $B_t = 2.54$ T.

When the plasma detachment is triggered by supplying the RMP field, the profiles of CIII–CVI completely change due to the formation of the m/n = 1/1 magnetic island and modification of the stochastic magnetic field lines in the ergodic layer. For both the 6-O and 7-O island cases, a new edge peak appears in the CIII and CIV profiles at the island location near $Z = \pm 400$ mm, while the original edge peak still remains at $Z \sim 420$ mm. Furthermore, the CIII and CIV emissions are also enhanced in the vicinity of edge X-points at $-400 \le Z \le -250$ mm for the 6-O island case and at $-300 \le Z \le 300$ mm for both the 6-O and 7-O island cases. On the other hand, the CV moves radially inside the plasma at the detachment phase but keeps the same vertical profile shape. This change is basically caused by the change in the T_e profile shown in Fig. 16(b).

It is already known that the CIII and CVI are localized in the temperature range of $T_e = 15$–20 eV.[32] The flattened electron temperature at the island location is in the range of $T_e = 10$–20 eV during the detachment phase (see Fig. 16(b)). This is the main reason why the CIII and CIV intensities are increased at the detachment phase. The intensity of CV is also stronger during the detachment phase, as well as the CIII and CIV intensities, while the intensity of CVI decreases. This indicates the enhancement of the impurity screening similar to that seen in the $R_{ax} = 3.75$ m case. Therefore, we conclude that the CIII–CV emissions located near the island can be selectively enhanced by the effect of the supplied RMP field, whereas the CVI emission decreases due to the enhanced impurity screening.

Since the changes in electron temperature and density modify the spatial distribution of carbon ions, it is important to independently study the effect of the RMP on the impurity transport. The simulation study on the spatial distribution of impurities is absolutely necessary for understanding the impurity transport during the detachment with the RMP field. At present, however, it is difficult to apply the EMC3-EIRENE code to plasmas with the stochastic magnetic field modified by the RMP field and the plasma pressure because the EMC3-EIRENE code has to be linked with another code, which can calculate the magnetic field structure without the assumption of MHD equilibrium. It will be a future work.

The vertical profiles of CIII−CVI at $R_{ax} = 3.90$ m without RMPs are compared between clockwise (solid lines) and counter-clockwise (dashed lines) B_t fields. The result is shown in Fig. 19. Similar to the previous result at $R_{ax} = 3.75$ m shown in Fig. 11, the up-down asymmetry is also observed in the CV and CVI vertical profiles. The simulation results

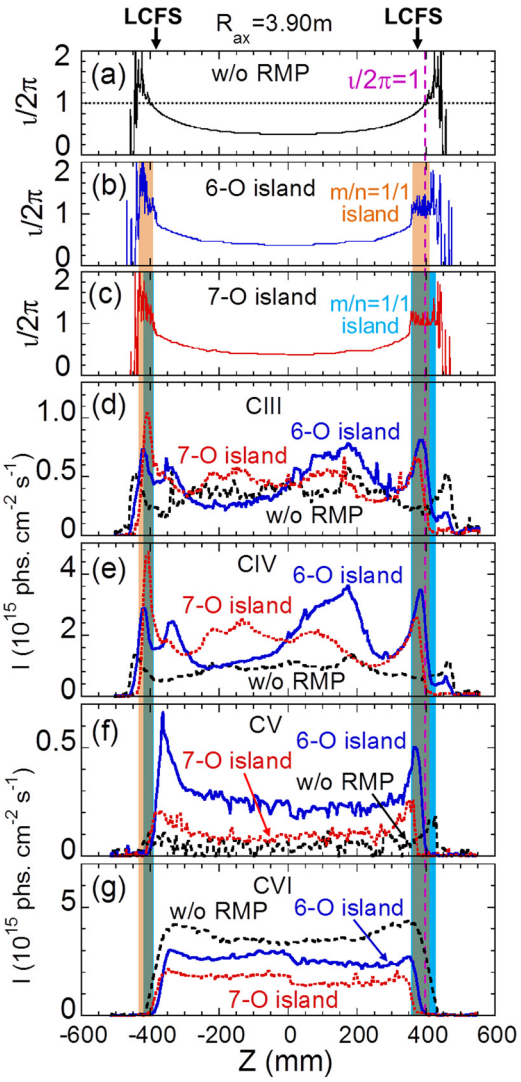


FIG. 18. $\iota/2\pi$ profiles (a) without RMP, (b) with 6-O island, (c) 7-O island, and vertical profiles of (d) CIII (386.203 Å), (e) CIV (384.174 Å), (f) CV (40.27 Å), and (g) CVI (33.73 Å) at the #10-O toroidal location in discharges at $R_{ax} = 3.90$ m without RMP (dashed line), with 6-O island (solid line), and with 7-O island (dotted line). Radial locations of LCFS and $\iota/2\pi = 1$ are indicated by vertical arrows and dashed line, respectively. The radial ranges of the m/n = 1/1 island are indicated by a shaded area with different colors for 6-O (brown) and 7-O island (sky blue).

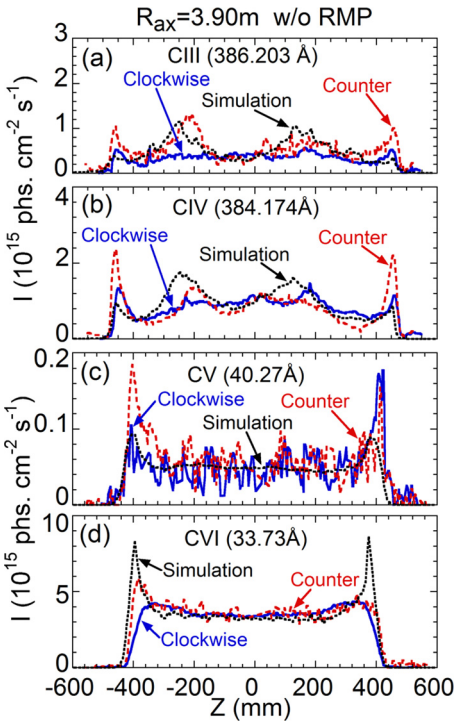


FIG. 19. Vertical profiles of (a) CIII (386.203 Å), (b) CIV (384.174 Å), (c) CV (40.27 Å), and (d) CVI (33.73 Å) measured at the #10-O toroidal location in discharges at $R_{ax} = 3.90$ m with a toroidal magnetic field in clockwise ($B_t = 2.54$ T: solid line) and counter-clockwise ($B_t = -2.54$ T: dashed line) directions and simulated with EMC3-EIRENE (dotted line).

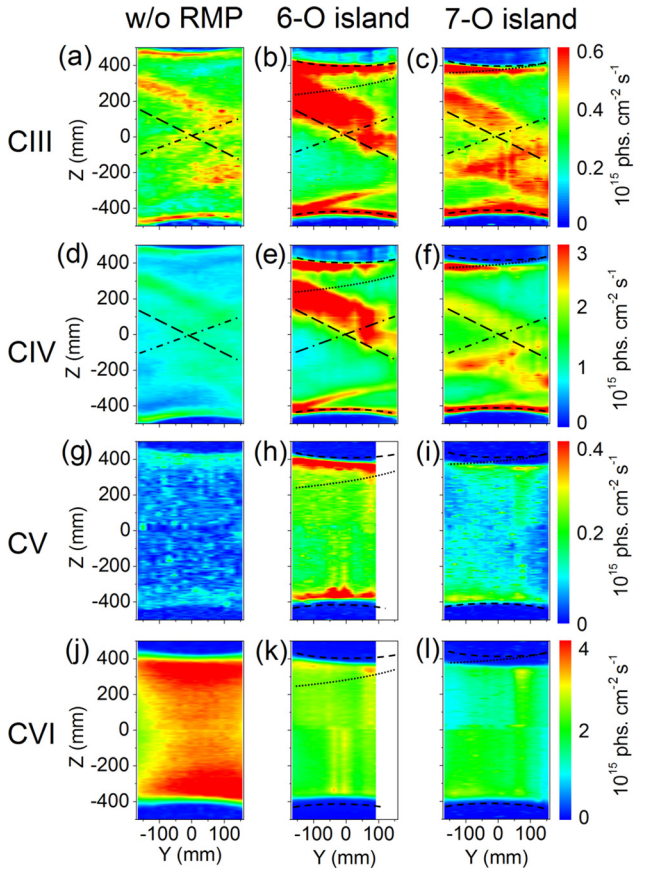


FIG. 20. 2-D distributions of CIII (386.203 Å) at $R_{ax} = 3.90$ m in discharges (a) without RMP, (b) with 6-O island, and (c) with 7-O island; CIV (384.174 Å) in discharges (d) without RMP, (e) with 6-O island, and (f) with 7-O island; CV (40.27 Å) in discharges (g) without RMP, (h) with 6-O island, and (i) with 7-O island; and CVI (33.73 Å) in discharges (j) without RMP, (k) with 6-O island, and (l) with 7-O island. Trajectories of the outboard X-point, inboard X-point, and island O-point are indicated by long dashed, dotted-dashed, and dashed lines, respectively. The radial location of $\iota/2\pi = 1$ is indicated by a dashed line.

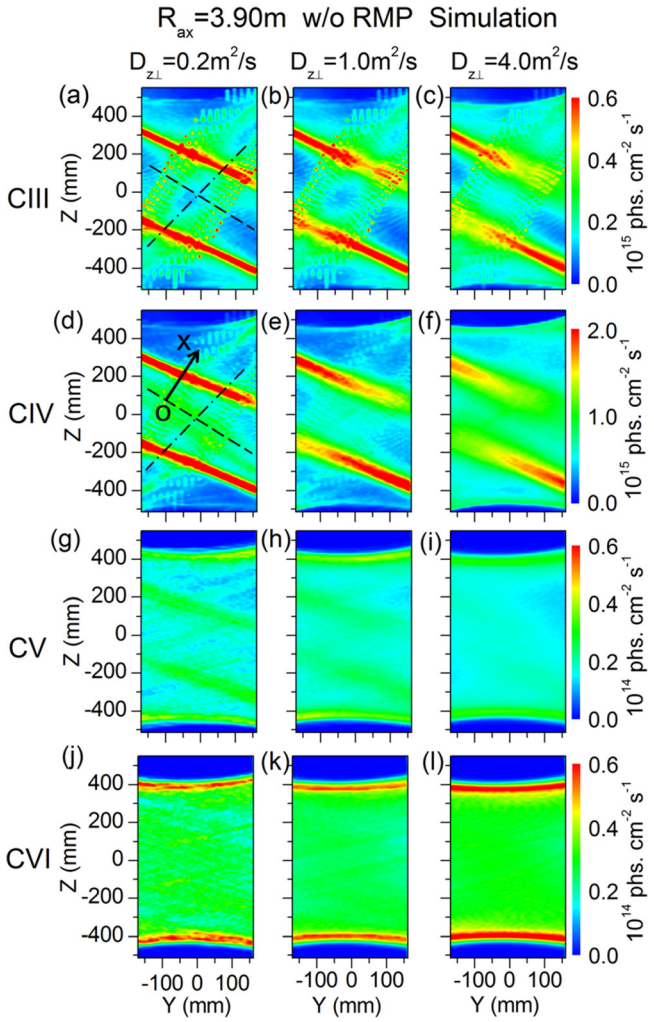


FIG. 21. 2-D emissivity distributions simulated with EMC3-EIRENE in $R_{ax} = 3.90$ m without RMP for (a) CIII (386.203 Å), (d) CIV (384.174 Å), (g) CV (40.27 Å), and (j) CVI (33.73 Å) at an impurity diffusion coefficient of $D_{Z\perp} = 0.2$ m^2/s, (b) CIII, (e) CIV, (h) CV, and (k) CVI at $D_{Z\perp} = 1.0$ m^2/s and (c) CIII, (f) CIV, (i) CV, and (l) CVI at $D_{Z\perp} = 4.0$ m^2/s. Trajectories of outboard and inboard X-points are indicated by long dashed and dotted-dashed lines, respectively. Coordinate x denoted in (d) defines the direction perpendicular to the outboard X-point trajectory as a reference point of (Y, Z) = (−100 mm, 100 mm) on the trajectory.

normalized at Z = 0 mm are denoted as dotted lines. The simulation shows a good agreement with the experiment when the value of $D_{Z\perp} = 4.0$ m^2/s is taken into account. The value of $D_{Z\perp}$ adopted here is 20 times larger than $D_{\perp} = 0.2$ m^2/s. Therefore, the simulated result indicates an extremely large impurity cross-field transport, at least, in the $R_{ax} = 3.90$ m configuration. The large difference between the experiment and simulation for CVI profiles also originates in the same reason as the former result in Fig. 11.

C. 2-D distribution of carbon line emissions

The 2-D distribution of carbon emissions is studied to understand further the detailed structural change in the edge carbon radiation during the plasma detachment phase. The 2-D distribution of CIII−VI is measured at the flattop during t = 6–8 s in Fig. 14 for the attached plasmas without RMP and the detached plasmas with 6-O and 7-O islands, as well as the $R_{ax} = 3.75$ m case. The result is shown in Fig. 20. The footprints of inboard and outboard X-points and island O-point are indicated by dashed-dotted, long-dashed, and dotted lines, respectively. The radial location of $\iota/2\pi = 1$ is also indicated by a short-dashed line.

In the attached plasma without RMP, the CIII and CIV shown in Figs. 20(a) and 20(d) are dominantly emitted in the top and bottom edges and the vicinity of outboard X-point denoted as a long-dashed line. In contrast to $R_{ax} = 3.75$ m, the CIII and CIV are only enhanced along the trace parallel to the outboard X-point at the upper half region. The CV and CVI emissions are considerably uniform. In order to understand these 2-D distributions, the simulation is done with EMC3-EIRENE for the attached plasmas without RMP, as shown in Fig. 21. The two enhanced strip-shaped emission traces parallel to the outboard X-point appear in the simulation for CIII and CIV emissions shown in Figs. 21(a) and 21(d), respectively. The upper emission trace in the simulation can also be seen in the measured CIII and CIV 2-D distributions (see Figs. 20(a) and 20(d)), whereas the lower emission trace almost disappears in the 2-D distribution. Although the reason for the asymmetric emission trace observed in the experiment is now unclear, it strongly suggests the necessity for additional

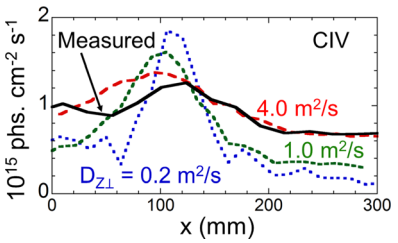


FIG. 22. Measured (solid line) and simulated CIV profiles as functions of x, which is denoted in Fig. 21(d). Simulations are carried out for three different impurity diffusion coefficients of $D_{Z\perp} = 0.2$ (dotted line), 1.0 (short-dashed line), and 4.0 m^2/s (long-dashed line).

concern regarding the physical mechanism in the simulation, e.g., particle drift. The 2-D plot of CVI simulation in Fig. 21(j) does not include the emission inside the LCFS as mentioned above.

The simulation is also carried out for three different impurity diffusion coefficients of $D_{Z\perp} = 0.2$, 1.0, and 4.0 m^2/s, as shown in Fig. 21. In order to determine the diffusion coefficient, the CIV profile perpendicular to the X-point footprint is compared between the measurement and simulation. Here, the coordinate x perpendicular to the outboard X-point footprint is defined as the reference point of (Y, Z) = (−100 mm, 100 mm), which is denoted by an arrow in Fig. 21(d). The measured perpendicular profile is plotted with the simulated profiles in Fig. 22 as a function of x. The measured profile seems to be wide, and the simulated profile becomes wider as $D_{Z\perp}$ increases. The experiment shows a good agreement with the simulated profile assuming $D_{Z\perp} = 4.0$ m^2/s. The impurity diffusion coefficient in the stochastic magnetic field layer obtained in the present analysis is 20 times bigger than the bulk ion diffusion coefficient, which is also obtained from the radial density profile in the plasma edge.

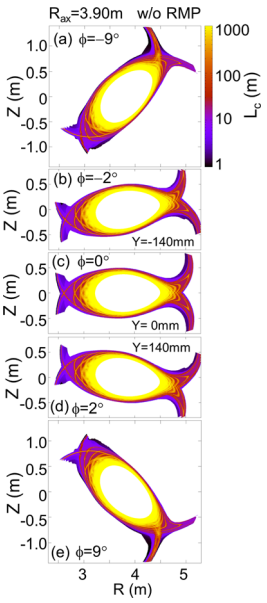


FIG. 23. Connection length, L_c, in the ergodic layer at $R_{ax} = 3.90$ m without RMP against five different toroidal angles of (a) $\phi = -9°$, (b) $\phi = -2°$, (c) $\phi = 0°$, (d) $\phi = 2°$, and (e) $\phi = 9°$. The poloidal cross section at toroidal angles of $\phi = -2°$, 0°, and 2° corresponds to the horizontal position of Y = −140 mm, 0, and 140 mm in the plot of 2-D distribution, respectively.

In addition, it is clear in Fig. 21 that the length of the two outboard strip-shaped emission traces, which appear in the 2-D distribution of CIII and CIV, is also sensitive to the diffusion coefficient. In order to explain why the length of two outboard traces changes with the diffusion coefficient, the poloidal distributions of magnetic field connection length, L_c, and simulated CIV emissivity at different toroidal angles, ϕ, are plotted in Figs. 23 and 24, respectively. As the toroidal angle moves from the horizontally elongated plasma position at $\phi = 0°$ to the vertically elongated plasma cross section at $\phi = -18°$ or 18°, the magnetic field structure near the outboard edge X-point becomes gradually asymmetric. The reason is explained in detail in Ref. 22. One of the two divertor legs at the outboard X-point tends to have longer L_c, i.e., upper divertor leg at $\phi = -9°$ in Fig. 23(a) and lower divertor leg at $\phi = 9°$ in Fig. 23(e).

The effect of impurity diffusion on the 2-D distribution of CIV is shown for two different $D_{Z\perp}$ values of 0.2 and 4.0 m^2/s in Figs. 24(a)–24(c) and 24(d)−24(f), respectively. The two arrows denote the vertical observation range. It is clearly shown that the CIV emissivity at the outboard side is much stronger than at the inboard side in the $R_{ax} = 3.90$ m configuration, and the CIV is distributed in a radially wider region when the $D_{Z\perp}$ is large. If the $D_{Z\perp}$ is larger at the shorter L_c region in the vicinity of the outboard X-point, the radially diffused carbon ions immediately move toward the divertor plates, and the emission intensity is resultantly weaker. The difference in the CIV emissivity between upper and lower sides of the outboard X-point is expressed in Figs. 24(d) and 24(f), which correspond to the horizontal position of Y = −140 and 140 mm in the 2-D plot, respectively. In addition, the chord integration length in CIV emissions above (below) the outboard X-point is longer than that below (above) the outboard X-point at $\phi = -2°$ ($\phi = 2°$). Therefore, the carbon intensity near the outboard X-point becomes different between the upper and lower sides as explained above. As a result, the CIII and CIV

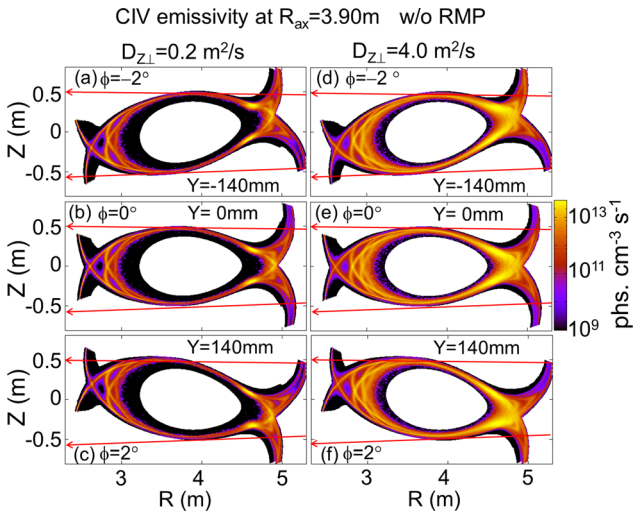


FIG. 24. Simulated poloidal distributions of CIV (384.174 Å) emissivity in the ergodic layer of $R_{ax} = 3.90$ m configuration without RMP at toroidal angles of (a) $\phi = -2°$, (b) $\phi = 0°$, and (c) $\phi = 2°$ with an impurity diffusion coefficient of $D_{Z\perp} = 0.2$ m^2/s and (d) $\phi = -2°$, (e) $\phi = 0°$, and (f) $\phi = 2°$ with $D_{Z\perp} = 4.0$ m^2/s. Observation chords of the EUV_Long2 spectrometer are indicated by arrows in each figure.

emissions are weaker in the upper strip-shaped emission trace at $Y = 140$ mm and lower strip-shaped emission trace at $Y = -140$ mm as shown in Fig. 21, when the $D_{Z\perp}$ is large. We thus understand that the length of the emission trace seen in Fig. 21 is a function of the diffusion coefficient. When we compare the CIII distribution in Figs. 21(a)–21(c) with Fig. 20(a) and the CIV distribution in Figs. 21(d)–21(f) with Fig. 20(d), the simulation with $D_{Z\perp} = 4.0$ m^2/s also seems to have a good agreement with the experiment.

Although the reason why the cross-field impurity transport in the fully stochastic magnetic field layer is so large is unclear at present, the Larmor radius of partially ionized carbon ions is at least larger than that of protons as the bulk ion, i.e., $\rho(C^{2+})/\rho(p) = 1.7$ and $\rho(C^{3+})/\rho(p) = 1.15$. A magnetic field deformation due to the plasma pressure seems to be very important because the effect is enhanced in the plasma edge.[33] Anomalous transport may also be important. The blob can create a perpendicular convective flux near the X-point with velocities of 0.1−1 km/s in LHD, which are clearly smaller than those of the blob in tokamaks, e.g., 2.5 km/s.[34] In addition, the direction of $E \times B$ force is frequently changeable in the stochastic magnetic field layer of LHD because the gradients of magnetic field strength and magnetic field curvature are considerably different due to the presence of a helical ripple. Since the perpendicular CIV profile is symmetric as shown in Fig. 22, the particle drift does not seem to sufficiently contribute to the large impurity diffusion coefficient.

When the plasma detachment occurs as a result of the RMP being applied, the CIII and CIV largely change their 2-D distributions and intensities. As shown in Figs. 20(b), 20(c), 20(e), and 20(f), the CIII and CIV intensities are drastically large at the top and bottom edges and along the outboard X-point. In addition, the intensities also become stronger at the upper-left corner in each figure, and those areas are close to the island location for both the 6-O and 7-O islands (also see Figs. 18(d) and 18(e)). The island can enhance the edge carbon emissions, of which the result is similar to the CVI case in $R_{ax} = 3.75$ m (see Figs. 10(f) and 12(i)). In other words, it also suggests that the RMP can create a sufficiently large island even in the ergodic layer. In the case of $R_{ax} = 3.90$ m, however, a new strip-shaped emission trace parallel to the inboard X-point footprint appears in the CIII and CIV 2-D distribution in the lower half of the figures. In particular, it is clear for the CIII distribution in Figs. 20(b) and 20(c). This suggests that the magnetic field structure in the ergodic layer is considerably modified by the external RMP field. In contrast, the 2-D distributions of CV and CVI do not obviously change even in the detached plasma, while the CV emission is stronger in the plasma edge and CVI emission becomes weaker at the detachment. The reduction in the CVI emission strongly suggests the enhancement of the edge impurity screening, which supports the result from the $R_{ax} = 3.75$ m configuration.

VI. SUMMARY

Vertical profiles and 2-D distributions of impurity carbon emissions (CIII–CVI) localized in the plasma edge have been studied in LHD to investigate the spatial structure during RMP-assisted detachment and the effect of the m/n = 1/1 magnetic island on the edge impurity distribution. The experiment is carried out in two different magnetic axis positions of $R_{ax} = 3.75$ m and 3.90 m in which the m/n = 1/1 magnetic island is located in the edge of the core plasma inside the LCFS and in the ergodic layer outside the LCFS, respectively.

In the $R_{ax} = 3.75$ m configuration, the structure of the CIV and CV emissions in the ergodic layer does not obviously change nor does the intensities when the RMP field is applied. The CVI mainly emitted inside the LCFS is enhanced only in the vicinity of the island O-point, while the total intensity itself is decreased due to the enhanced impurity screening. Therefore, the formation of plasma detachment using the RMP field seems to be difficult in the case of $R_{ax} = 3.75$ m configuration because the magnetic island only affects the edge region of the core plasma. The CIII−CVI emissions at $R_{ax} = 3.75$ m are simulated with a 3-D edge plasma transport code, EMC3-EIRENE, for the attached plasmas without RMP, while the simulation for detached plasmas with RMP is not done because the code cannot treat the stochastic magnetic field layer with an external magnetic field at present. These simulation results confirm that the poloidal distributions of CIII and CIV are entirely non-uniform, with enhanced intensity in the vicinity of inner and outer X-points, whereas the CV and CVI intensities show a uniform poloidal distribution.

In the $R_{ax} = 3.90$ m configuration, on the other hand, the plasma detachment occurs when the m/n = 1/1 island is formed in the vicinity of the LCFS including the ergodic layer. An electron temperature flattening appears in the plasma edge during the detachment, and the temperature is in the range of $10 \leq T_e \leq 20$ eV. It is found that the CIII and CIV are significantly enhanced in the vicinity of the island O-point and both inboard and outboard edge X-points during the plasma detachment phase and are located in the radial position with the temperature flattening, while the CVI emission located inside the island decreases due to the enhancement of edge impurity screening. 2-D distributions of carbon ions are also simulated with EMC3-EIRENE in the $R_{ax} = 3.90$ m configuration without RMP. The results confirm that the non-uniform poloidal distributions of CIII and CIV are enhanced in the vicinity of outboard X-points.

In the simulation, two strip-shaped emission traces appeared at the upper and lower sides of X-points along the outboard edge X-point footprint, while in the experiment, only a single emission trace is observed at the upper side. It is found that both the width and the length of the strip-shaped emission trace are sensitive to the impurity cross-field transport coefficient. Then, the cross-field carbon diffusion coefficient is analyzed from the observed width and length of the emission trace by comparing with the simulation. As a result, we understand that the cross-field diffusion coefficient, $D_{Z\perp}$, is more significant in the $R_{ax} = 3.90$ m configuration than in the $R_{ax} = 3.75$ m configuration. The cross-field diffusion coefficient at $R_{ax} = 3.90$ m is determined to be $D_{Z\perp} = 4.0$ m^2/s, while the $D_{Z\perp}$ at $R_{ax} = 3.75$ m is only 5 times larger than that of the bulk plasma ($D_\perp = 0.2$ m^2/s). The difference of $D_{Z\perp}$

between $R_{ax} = 3.75$ m and 3.90 m configurations seems to depend on how the magnetic field is stochastic, in other words, degree of stochasticity.

ACKNOWLEDGMENTS

The authors thank all members of the LHD experimental group for their technical support and Professor Yokoyama for the calculation of NBI deposition power. This work was partially carried out under the LHD project financial support (NIFS16ULPP010). This work was also partly supported by the JSPS KAKENHI Grant Nos. 16H04088 and JSPS-NRF-NSFC A3 Foresight Program in the field of Plasma Physics (NSFC: No. 11261140328 and NRF: No. 2012K2A2A6000443).

[1]ITER Physics Basis, "Chapter 4: Power and particle control," Nucl. Fusion **39**, 2391 (1999).
[2]M. Shimada, D. J. Campbell, V. Mukhovatov, M. Fujiwara, N. Kirneva, K. Lackner, M. Nagami, V. D. Pustovitov, N. Uckan, and J. Wesley, Nucl. Fusion **47**, S1–S17 (2007).
[3]A. Loarte, B. Lipschultz, A. S. Kukushkin, G. F. Matthews, P. C. Stangeby, N. Asakura, G. F. Counsell, G. Federici, A. Kallenbach, K. Krieger, A. Mahdavi, V. Philipps, D. Reiter, J. Roth, J. Strachan, D. Whyte, R. Doerner, T. Eich, W. Fundamenski, A. Herrmann, M. Fenstermacher, P. Ghendrih, M. Groth, A. Kirschner, S. Konoshima, B. LaBombard, P. Lang, A. W. Leonard, P. Monier-Garbet, R. Neu, H. Pacher, B. Pegourie, R. A. Pitts, S. Takamura, J. Terry, E. Tsitrone, and ITPA Scrape-off Layer and Divertor Physics Topical Group, Nucl. Fusion **47**, S203–S263 (2007).
[4]Y. Shimomura, M. Keilhacker, K. Lackner, and H. Murmann, Nucl. Fusion **23**, 869 (1983).
[5]O. Gruber, A. Kallenbach, M. Kaufmann, K. Lackner, V. Mertens, J. Neuhauser, F. Ryter, H. Zohm, M. Bessenrodt-Weberpals, K. Büchl, S. Fiedler, A. Field, Ch. Fuchs, C. Garcia-Rosales, G. Haas, A. Herrmann, W. Herrmann, S. Hirsch, W. Köppendörfer, P. Lang, G. Lieder, K.-F. Mast, C. S. Pitcher, M. Schittenhelm, J. Stober, W. Suttrop, M. Troppmann, M. Weinlich, M. Albrecht, M. Alexander, K. Asmussen, M. Ballico, K. Behler, K. Behringer, H. S. Bosch, M. Brambilla, A. Carlson, D. Coster, L. Cupido, H. J. DeBlank, S. De Pena Hempel, S. Deschka, C. Dorn, R. Drube, R. Dux, A. Eberhagen, W. Engelhardt, H.-U. Fahrbach, H.-U. Feist, D. Fieg, G. Fußmann, O. Gehre, J. Gernhardt, P. Ignacz, B. Jüttner, W. Junker, T. Kass, K. Kiemer, H. Kollotzek, M. Kornherr, K. Krieger, B. Kurzan, R. Lang, M. Laux, M. E. Manso, M. Maraschek, H.-M. Mayer, P. McCarthy, D. Meisel, R. Merkel, H. Murmann, B. Napiontek, D. Naujoks, G. Neu, R. Neu, J.-M. Noterdaeme, G. Pautasso, W. Poschenrieder, G. Raupp, H. Richter, T. Richter, H. Röhr, J. Roth, N. Salmon, H. Salzmann, W. Sandmann, H.-B. Schilling, H. Schneider, R. Schneider, W. Schneider, K. Schönmann, G. Schramm, U. Schumacher, J. Schweinzer, U. Seidel, F. Serra, A. Silva, M. Sokoll, E. Speth, A. Stäbler, K.-H. Steuer, B. Streibl, W. Treutterer, M. Ulrich, P. Varela, H. Vernickel, O. Vollmer, H. Wedler, U. Wenzel, F. Wesner, R. Wunderlich, D. Zasche, and H. P. Zehrfeld, Phys. Rev. Lett. **74**, 4217 (1995).
[6]F. Reimold, M. Wischmeier, M. Bernert, S. Potzel, A. Kallenbach, H. W. Müller, B. Sieglin, U. Stroth, and ASDEX Upgrade Team, Nucl. Fusion **55**, 033004 (2015).
[7]T. W. Petrie, M. R. Wade, N. H. Brooks, M. E. Fenstermacher, M. Groth, A. W. Hyatt, R. C. Isler, C. J. Lasnier, A. W. Leonard, M. A. Mahdavi, G. D. Porter, M. J. Schaffer, J. G. Watkins, W. P. West, and DIII–D Team, J. Nucl. Mater. **363–365**, 416–420 (2007).
[8]T. Nakano, N. Asakura, H. Kubo, and JT-60 Team, J. Nucl. Mater. **438**, S291–S296 (2013).
[9]A. Huber, S. Brezinsek, M. Groth, P. C. de Vries, V. Riccardo, G. van Rooij, G. Sergienko, G. Arnoux, A. Boboc, P. Bilkova, G. Calabro, M. Clever, J. W. Coenen, M. N. A. Beurskens, T. Eich, S. Jachmich, M. Lehnen, E. Lerche, S. Marsen, G. F. Matthews, K. McCormick, A. G. Meigs, Ph. Mertens, V. Philipps, J. Rapp, U. Samm, M. Stamp, M. Wischmeier, S. Wiesen, and JET-EFDA Contributors, J. Nucl. Mater. **438**, S139–S147 (2013).
[10]B. Lipschultz, B. LaBombard, J. L. Terry, C. Boswell, and I. H. Hutchinson, Fusion Sci. Technol. **51**, 369–389 (2007).
[11]N. Asakura, H. Hosogane, S. Tsuji-Iio, K. Itami, K. Shimizu, and M. Shimada, Nucl. Fusion **36**, 795 (1996).
[12]M. Kobayashi, S. Masuzaki, I. Yamada, N. Tamura, Y. Feng, K. Sato, M. Goto, Y. Narushima, T. Akiyama, J. Miyazawa, M. Shoji, S. Morita, B. J. Peterson, H. Funaba, N. Ohyabu, K. Narihara, T. Morisaki, H. Yamada, A. Komori, LHD Experimental Group, and D. Reiter, Phys. Plasmas **17**, 056111 (2010).
[13]P. Grigull, K. McCormick, Y. Feng, A. Werner, R. Brakel, H. Ehmler, F. Gadelmeier, D. Hartmann, D. Hildebrandt, R. Jaenicke, J. Kisslinger, T. Klinger, R. König, D. Naujoks, H. Niedermeyer, F. Sardei, F. Wagner, U. Wenzel, and W7-AS Team, J. Nucl. Mater. **313–316**, 1287 (2003).
[14]Y. Feng, F. Sardei, J. Kisslinger, P. Grigull, K. McCormick, D. Reiter, L. Giannone, R. Koenig, N. Ramasubramanian, H. Thomsen, and U. Wenzel, Nucl. Fusion **45**, 89 (2005).
[15]S. Morita, C. F. Dong, M. Kobayashi, M. Goto, X. L. Huang, I. Murakami, T. Oishi, E. H. Wang, N. Ashikawa, K. Fujii, M. Hasuo, H. Kasahara, D. Kato, F. Koike, S. Masuzaki, H. A. Sakaue, T. Shikama, N. Yamaguchi, and LHD Experiment Group, Nucl. Fusion **53**, 093017 (2013).
[16]C. F. Dong, S. Morita, M. Goto, and H. Y. Zhou, Rev. Sci. Instrum. **81**, 033107 (2010).
[17]E. H. Wang, S. Morita, M. Goto, and C. F. Dong, Rev. Sci. Instrum. **83**, 043503 (2012).
[18]H. M. Zhang, S. Morita, T. Oishi, M. Kobayashi, M. Goto, and X. L. Huang, Jpn. J. Appl. Phys., Part 1 **54**, 086101 (2015).
[19]M. B. Chowdhuri, S. Morita, M. Kobayashi, M. Goto, H. Y. Zhou, S. Masuzaki, T. Morisaki, K. Narihara, I. Yamada, and Y. H. Feng, Phys. Plasmas **16**, 062502 (2009).
[20]A. Komori, H. Yamada, S. Sakakibara, O. Kaneko, K. Kawahata, T. Mutoh, N. Ohyabu, S. Imagawa, K. Ida, Y. Nagayama, T. Shimozuma, K. Y. Watanabe, T. Mito, M. Kobayashi, K. Nagaoka, R. Sakamoto, N. Yoshida, S. Ohdachi, N. Ashikawa, Y. Feng, T. Fukuda, H. Igami, S. Inagaki, H. Kasahara, S. Kubo, R. Kumazawa, O. Mitarai, S. Murakami, Y. Nakamura, M. Nishiura, T. Hino, S. Masuzaki, K. Tanaka, K. Toi, A. Weller, M. Yoshinuma, Y. Narushima, N. Ohno, T. Okamura, N. Tamura, K. Saito, T. Seki, S. Sudo, H. Tanaka, T. Tokuzawa, N. Yanagi, M. Yokoyama, Y. Yoshimura, T. Akiyama, H. Chikaraishi, M. Chowdhuri, M. Emoto, N. Ezumi, H. Funaba, L. Garcia, P. Goncharov, M. Goto, K. Ichiguchi, M. Ichimura, H. Idei, T. Ido, S. Iio, K. Ikeda, M. Irie, A. Isayama, T. Ishigooka, M. Isobe, T. Ito, K. Itoh, A. Iwamae, S. Hamaguchi, T. Hamajima, S. Kitajima, S. Kado, D. Kato, T. Kato, S. Kobayashi, K. Kondo, S. Masamune, Y. Matsumoto, N. Matsunami, T. Minami, C. Michael, H. Miura, J. Miyazawa, N. Mizuguchi, T. Morisaki, S. Morita, G. Motojima, I. Murakami, S. Muto, K. Nagasaki, N. Nakajima, Y. Nakamura, H. Nakanishi, H. Nakano, K. Narihara, A. Nishimura, H. Nishimura, K. Nishimura, S. Nishimura, N. Nishino, T. Notake, T. Obana, K. Ogawa, Y. Oka, T. Ohishi, H. Okada, K. Okuno, K. Ono, M. Osakabe, T. Osako, T. Ozaki, B. J. Peterson, H. Sakaue, M. Sasao, S. Satake, K. Sato, M. Sato, A. Shimizu, M. Shiratani, M. Shoji, H. Sugama, C. Suzuki, Y. Suzuki, K. Takahata, H. Takahashi, Y. Takase, Y. Takeiri, H. Takenaga, S. Toda, Y. Todo, M. Tokitani, H. Tsuchiya, K. Tsumori, H. Urano, E. Veshchev, F. Watanabe, T. Watanabe, T. H. Watanabe, I. Yamada, S. Yamada, O. Yamagishi, S. Yamaguchi, S. Yoshimura, T. Yoshinaga, and O. Motojima, Nucl. Fusion **49**, 104015 (2009).
[21]N. Ohyabu, T. Watanabe, H. Ji, K. Yamazaki, K. Akaishi, N. Inoue, A. Komori, Y. Kubota, N. Noda, A. Sagara, H. Suzuki, O. Motojima, M. Fujiwara, and A. Iiyoshi, Nucl. Fusion **34**, 387 (1994).
[22]S. Morita, E. H. Wang, M. Kobayashi, C. F. Dong, T. Oishi, Y. Feng, M. Goto, X. L. Huang, S. Masuzaki, I. Murakami, Y. Suzuki, T. Watanabe, and LHD Experiment Group, Plasma Phys. Controlled Fusion **56**, 094007 (2014).
[23]M. B. Chowdhuri, S. Morita, M. Goto, H. Nishimura, K. Nagai, and S. Fujioka, Rev. Sci. Instrum. **78**, 023501 (2007); Erratum **84**, 109901 (2013).
[24]M. B. Chowdhuri, S. Morita, and M. Goto, Appl. Opt. **47**, 135–146 (2008).
[25]T. Oishi, S. Morita, X. L. Huang, H. M. Zhang, M. Goto, and LHD Experiment Group, Plasma Fusion Res. **10**, 3402031 (2015).
[26]X. L. Huang, S. Morita, T. Oishi, M. Kobayashi, M. Goto, and H. M. Zhang, Rev. Sci. Instrum. **85**, 043511 (2014).

[27]C. F. Dong, S. Morita, M. Goto, and E. H. Wang, Rev. Sci. Instrum. **82**, 113102 (2011).
[28]Y. Feng, F. Sardei, J. Kisslinger, P. Grigull, K. McCormick, and D. Reiter, Contrib. Plasma Phys. **44**, 57 (2004).
[29]D. Reiter, M. Baelmans, and P. Boerner, Fusion Sci. Technol. **47**, 172 (2005).
[30]S. Y. Dai, M. Kobayashi, G. Kawamura, S. Morita, T. Oishi, H. M. Zhang, X. L. Huang, Y. Feng, D. Z. Wang, Y. Suzuki, and LHD Experiment Group, Contrib. Plasma Phys. **56**, 628–633 (2016).
[31]S. Y. Dai, M. Kobayashi, G. Kawamura, S. Morita, H. M. Zhang, T. Oishi, Y. Feng, D. Z. Wang, Y. Suzuki, and LHD Experimental Group, Nucl. Fusion **56**, 066005 (2016).
[32]H. M. Zhang, S. Morita, T. Oishi, I. Murakami, X. L. Huang, and M. Goto, Plasma Fusion Res. **11**, 2402019 (2016).
[33]Y. Suzuki, K. Y. Watanabe, H. Funaba, S. Sakakibara, N. Nakajima, N. Ohyabu, and LHD Experiment Group, Plasma Fusion Res. **4**, 036 (2009).
[34]H. Tsuchiya, T. Morisaki, V. P. Budaev, A. Komori, and H. Yamada, Plasma Fusion Res. **5**, S2078 (2010).